2012

Infrared Tapered Slot Antennas Coupled To Tunnel Diodes

Louis A. Florence
University of Central Florida

INFRARED TAPERED SLOT ANTENNAS COUPLED TO TUNNEL DIODES

by

LOUIS A. FLORENCE
B.S. United States Military Academy, 1993
M.S. University of Rochester, 2002

A proposal for dissertation submitted in partial fulfillment of the requirements
for the degree of Doctor of Philosophy
in the College of Optics and Photonics: CREOL & FPCE
at the University of Central Florida
Orlando, Florida

Summer Term
2012

Major Professor: Glenn D. Boreman

ABSTRACT

Tapered slot antennas (TSAs) have seen considerable application in the millimeter-wave portion of the spectrum. Desirable characteristics of TSAs include symmetric E- and H-plane antenna patterns, and broad non-resonant bandwidths. We investigate extension of TSA operation toward higher frequencies in the thermal infrared (IR), using a metal-oxide-metal diode as the detector. Several different infrared TSA design forms are fabricated using electron-beam lithography and specially developed thin-film processes. The angular antenna patterns of TSA-coupled diodes are measured at 10.6 micrometer wavelength in both E- and H-planes, and are compared to results of finite-element electromagnetic modeling using Ansoft HFSS. Parameter studies are carried out, correlating the geometric and material properties of several TSA design forms to numerical-model results and to measurements. A significant increase in antenna gain is noted for a dielectric-overcoat design. The traveling-wave behavior of the IR TSA structure is investigated using scattering near-field microscopy. The measured near-field data is compared to HFSS results. Suggestions for future research are included

To Vanessa, Kevin, Aaron, Ryan and Delaney

TABLE OF CONTENTS

LIST OF FIGURES

LIST OF TABLES

CHAPTER ONE: TAPERED SLOT ANTENNA

1.1 Introduction to Endfire Antennas

In its most general form, a tapered slot antenna is any metallic, planar antenna consisting of a slotline that gradually expands in the (endfire) direction of radiation. The concept of a planar endfire antenna is the natural extension of the three-dimensional horn antennas used by millimeter wave community for decades. The planar nature of the antenna allows it to be directly integrated into microwave circuitry. P.J. Gibson reported the first tapered slot antenna in his 1979 conference presentation, "The Vivaldi Aerial" [1]. His device operated in the 8-40 GHz frequency range (7.5 mm to 37.5mm). It consisted of an exponential taper pattern lithographically placed onto an alumina substrate. Designed to have a "theoretically unlimited instantaneous bandwidth"[1], it also exhibited a rotationally-symmetric beam pattern, which is counterintuitive for a planar antenna. These properties, coupled with claims of high gain and polarization rejection, made the tapered slot antenna a desirable alternative to dipole antennas.

These findings resulted in a rapid development of other types of TSAs. Prasad and Mahapatra introduced the linear TSA at the same conference in 1979 [2]. Their antenna used a linearly broadened slotline instead of an exponentially broadened slotline at the expense of bandwidth, but with narrower radiation patterns. In 1985, the constant-width slot antenna was introduced by Yngvesson, et al [3]. This antenna consisted of a slotline that rapidly tapered into a much wider slotline, but maintained a rectangular slot appearance. Top view diagrams of the three types of antenna are shown in Fig. 1. Other antennas consisting of portions of these three antenna designs have been proposed for various studies, but will not be discussed here [4-7].

All versions of the TSA have several common characteristics considered desirable. They are broad bandwidth devices, with symmetric radiation patterns. They are lightweight, and are ready for coupling into other devices because of their slotline termination. Because they are small (transverse dimensions are on the order of a few wavelengths), they can be packed into dense focal plane arrays for imaging. Because they are flat, they are readily integrated into circuits on the same substrate [8].

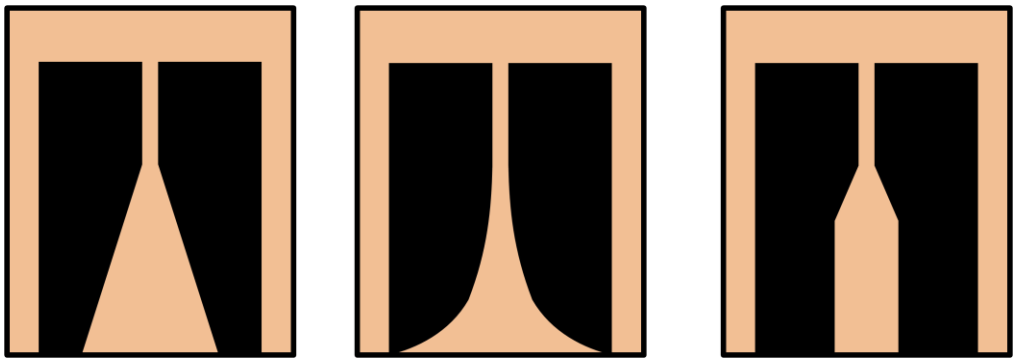

Figure 1. Endfire antenna geometries: (a) Linear Tapered Slot, (b) Vivaldi or Exponential Tapered Slot, and (c) Constant-Width Tapered Slot.

1.2 Linear Tapered Slot Antenna Design Parameters

The linear tapered slot antenna consists of a metal plane with a slotline, where the slotline broadens linearly into an aperture in the direction of endfire radiation. Antenna dimensions are on the order of a few wavelengths. Fig. 2 shows the critical dimensions for the antenna. These antennas are designed to optimize directionality (as measured by their -3dB angular width and small sidelobes), and for their rotational symmetry (as measured by their E-plane and H-plane -3dB angular width). The E-plane is defined as the TE plane at the elevation angle of maximum

response, which would be the plane of the antenna for an endfire TSA; the H-plane is orthogonal to the E-plane, and bisects the slotline.

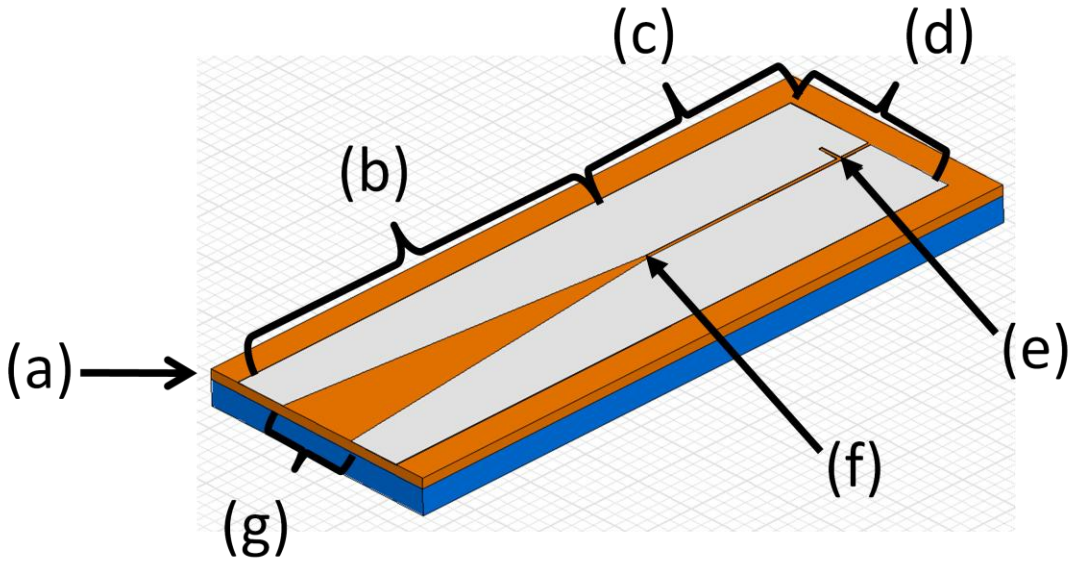

	Parameter	Typical Value Range
a	Substrate thickness (t_o)	$0.005\lambda_o<t_{eff}<0.03\ \lambda_o$; $t_{eff} = \sqrt{\epsilon_r - 1}t_o$
b	Taper length	>2 Wavelengths
c	Slotline length and width	Length not reported Width <0.1 Wavelengths
d	Antenna width	>3 Wavelengths
e	Cross-piece size and location	Not reported
f	Diode location	Near the taper apex
g	Aperture width	>one-half wavelength

Figure 2. TSA critical parameters and typical values.

For devices that operate at higher frequencies than millimeter-wave, structural support for the antenna becomes an issue. The metal planes of the antenna require some substrate to provide this structural support, and this substrate changes the waveguide properties of the antenna [9]. At millimeter wavelengths, substrates can be millimeters thick to provide this structural support without affecting the antenna properties. Additionally, the substrates can be machined to further reduce the dielectric constant as a volumetric average [9-11]. At infrared frequencies, the substrate is limited to a maximum thickness of several microns before the antenna properties are affected. Manipulating such a thin substrate and maintaining some structural strength is very challenging. The solution to this requirement for a thin substrate in the infrared. seems to be a combination of mechanical methods, novel materials, and photonic structures. This shall be discussed in greater detail in Chapter 7.

1.3 Analytical Solutions for Millimeter Wave Fields

The TSA is a travelling wave antenna, and therefore does not lend itself to a resonance-based analysis. Thus, the mathematic treatment of traditional resonant antenna systems does not apply to the TSA. Because the initial development and improvements were performed empirically, the analytical modeling of the far-field radiation pattern of the TSA was delayed until 1987. In 1969, Seymour B. Cohn developed an analytic solution for the wavelength, impedance, phase velocity and group velocity of radiation inside a straight slotline on a dielectric [12]. Ramakrishna Janaswamy and Daniel Schaubert furthered the work of Cohn to include the effects of various width values and dielectric constants of thin substrates on the impedance and effective wavelength of the slotline [13-15]. They then applied these results to a tapered slotline by modeling the tapered region as consisting of slotlines of various widths (Fig. 3) [16]. The

resulting far-field pattern would be the summation of radiation patterns from each segment. This method is presented here in an attempt to determine the effects of various parameters on the far field radiation pattern. It should be noted that although a linear tapered slot is shown, this method is also applicable to exponentially tapered slot antennas.

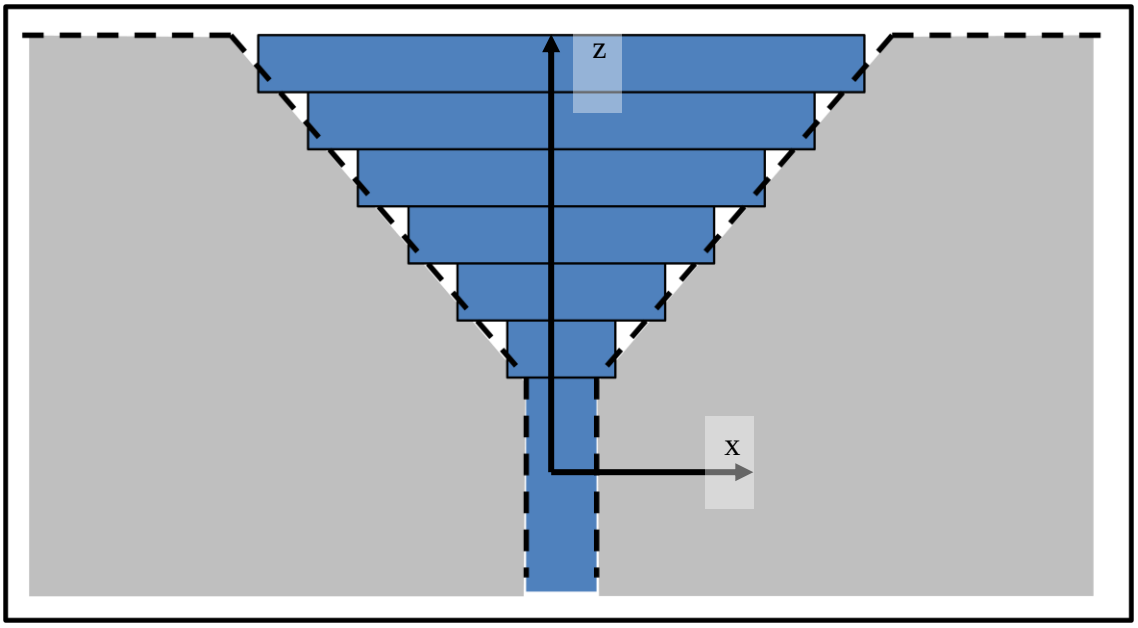

Figure 3. Segmented antenna model used to find an analytical solution.

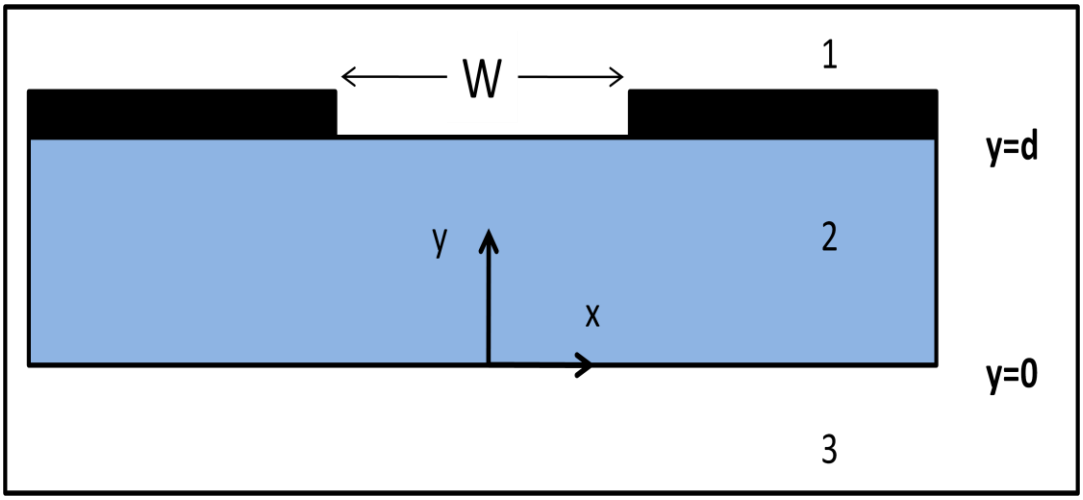

Figure 4. Side-view of slotline for use in analytical solution. The black bars on top are the metal surfaces that form the planar slot.

Fig. 4 shows the geometry and boundaries used throughout the analysis. It should be noted that region 3 is assumed to be air, and region 2 is a thin dielectric. This is not the case with infrared TSAs, as the thin films (region 2) cannot mechanically support the antenna and diode and therefore require a substrate. An example substrate is silicon, which has a high refractive index in the infrared.

The electric and magnetic scalar potentials in the three regions (air, substrate, air) can be written [8]:

$$\tilde{\Phi}_1^{\mathrm{e}}(\eta, y) = A^e(\eta) e^{-\gamma_1 (y-d)} \tag{1}$$

$$\tilde{\Phi}_2^{\mathrm{e}}(\eta, y) = B^e(\eta) sinh(\gamma_2 y) + C^e(\eta) cosh(\gamma_2 y) \tag{2}$$

$$\tilde{\Phi}_3^{\mathrm{e}}(\eta, y) = D^e(\eta) e^{\gamma_3 y} \tag{3}$$

$$\tilde{\Phi}_1^{\mathrm{h}}(\eta, y) = A^h(\eta) e^{-\gamma_1 (y-d)} \tag{4}$$

$$\tilde{\Phi}_2^{\mathrm{h}}(\eta, y) = B^h(\eta) sinh(\gamma_2 y) + C^h(\eta) cosh(\gamma_2 y) \tag{5}$$

$$\widetilde{\Phi}_3^{\mathrm{h}}(\eta, y) = D^h(\eta) e^{\gamma_3 y} \tag{6}$$

The subscripts denote the medium (1, 2, or 3) as depicted in Fig. 4. The superscript specifies either the electric (e) or magnetic (h) potential. Note that the transverse component (x) has been converted to its spatial frequency, η.

These potentials are related to the fields in each medium as [8]

$$\tilde{E}_{zi}(\eta, y, z) = \frac{k_i^2 - k_z^2}{jk_z} \widetilde{\Phi}_{\mathrm{i}}^{\mathrm{e}}(\eta, y) e^{-jk_z z} \tag{7}$$

$$\widetilde{H}_{zi}(\eta, y, z) = \frac{k_i^2 - k_z^2}{jk_z} \widetilde{\Phi}_{\mathrm{i}}^{\mathrm{h}}(\eta, y) e^{-jk_z z} \tag{8}$$

$$\tilde{E}_{xi}(\eta, y, z) = \left(-\mathrm{j}\eta \widetilde{\Phi}_{\mathrm{i}}^{\mathrm{e}}(\eta, y) - \frac{z_i}{jk_z} \frac{\partial \widetilde{\Phi}_{\mathrm{i}}^{\mathrm{h}}(\eta, y)}{\partial y} \right) e^{-jk_z z} \tag{9}$$

$$\widetilde{H}_{xi}(\eta, y, z) = \left(\frac{y_i}{jk_z} \frac{\partial \widetilde{\Phi}_{\mathrm{i}}^{\mathrm{e}}(\eta, y)}{\partial y} - \mathrm{j}\eta \widetilde{\Phi}_{\mathrm{i}}^{\mathrm{h}}(\eta, y) \right) e^{-jk_z z} \tag{10}$$

where k_z is the unknown wave vector magnitude in the z-direction. The variable k_i is the effective wave vector magnitude in the i[th] segment of the slotline ($k_i = \omega\sqrt{\varepsilon_i \mu_i}$). The variables z_i and y_i are related to the permeability and the permittivity of the slot, respectively ($z_i = j\omega\mu_i$ and $y_i = j\omega\varepsilon_i$).

These fields are limited by the following boundary conditions:

At y=0 (substrate-air interface)

$$E_{z2} = E_{z3} \qquad E_{x2} = E_{x3} \qquad -\infty < x < \infty \tag{11}$$

$$H_{z2} = H_{z3} \qquad H_{x2} = H_{x3} \tag{12}$$

At y=d (substrate-slot/conductor interface)

$$E_{z1} = E_{z2} \qquad E_{x1} = E_{x2} \qquad -\infty < x < \infty \tag{13}$$

$$E_{z1} = \begin{cases} 0, |x| \geq {}^{w}/_{2} \\ e_z(x), |x| \leq {}^{w}/_{2} \end{cases} \quad (14)$$

$$E_{x1} = \begin{cases} 0, |x| \geq {}^{w}/_{2} \\ e_x(x), |x| \leq {}^{w}/_{2} \end{cases} \quad (15)$$

$$H_{z1} = \begin{cases} j_x(x), |x| \geq {}^{w}/_{2} \\ 0, |x| \leq {}^{w}/_{2} \end{cases} \quad (16)$$

$$H_{x1} - H_{x2} = \begin{cases} j_z(x), |x| \geq {}^{w}/_{2} \\ 0, |x| \leq {}^{w}/_{2} \end{cases} \quad (17)$$

where w is the slot width, $e_p(x)$ is the unknown electric field polarized in the p-direction in the slot, and $j_p(x)$ is the unknown surface current component.

Applying the boundary conditions, one can solve for all of the unknown coefficients in terms of $\xi_x(\eta)$ and $\xi_z(\eta)$ (the Fourier transforms of the fields in the slot), and $J_x(\eta)$ and $J_z(\eta)$ (the Fourier transforms of the surface current in the metal). Thus, there are two equations with four unknowns:

$$\Gamma_1(\eta, k_z)\xi_z(\eta) + \Gamma_2(\eta, k_z)\xi_x(\eta) = e^{j\eta w/2}J_x(\eta) + e^{-j\eta w/2}J_x(-\eta) \quad (18)$$

$$\Gamma_3(\eta, k_z)\xi_z(\eta) + \Gamma_4(\eta, k_z)\xi_x(\eta) = e^{j\eta w/2}J_z(\eta) + e^{-j\eta w/2}J_z(-\eta) \quad (19)$$

Here, Γ_n are known functions of η and k_z [8].

To solve the equations for the field, Galerkin's method is applied to the slot field written as a linear combination of Chebyshev polynomials. When the phase is included, the transverse slot field can be written [8,15]

$$e_x^i(x,y) \triangleq e^{jk_z^i z}\left(\frac{2\sqrt{Z_o^i}}{\pi w^i}\right)\sum_{n=1}^{\infty}\frac{a_n^i T_{2(n-1)}\left(\frac{2x}{w^i}\right)}{\sqrt{1-\left(\frac{2x}{w}\right)^2}} \tag{20}$$

The impedance of the ith segment Z_o is found by integrating the transverse component of the electric field across the slot to determine the voltage, squaring the voltage, and dividing the voltage squared by the average power flow along the slotline. This average power flow is the integration of the Poynting vector across one facet of the segment [13].

The far field electric field contribution from the i[th] section can be found by integrating the slot field multiplied by the pattern function for a two-sided slot cut in a semi-infinte conducting plane. (Note that this function assumes the dielectric does not impact the pattern.) [8]

$$E_\theta^i(\theta,\phi) = \int_{S_i} g_\theta(\theta,\phi)e_x^i(x,z)dS \tag{21}$$

$$g_\theta(\theta,\phi) = |sin\phi|e^{j\pi/4}F(v)e^{jk_o(zsin\theta cos\phi + xcos\theta)} + \frac{sin\left(\phi/2\right)e^{-j[\pi/4 + k_o(zsin\theta - xcos\theta)]}}{\sqrt{\pi k_o zsin\theta}} \tag{22}$$

Here, *F(v)* is the Fresenel integral

$$F(v) = \int_0^v \frac{e^{-jt}}{\sqrt{2\pi t}}dt \tag{23}$$

and *v* is a substitution

$$v = k_o zsin\theta(1 + cos\phi)) \tag{24}$$

Jamaswany and Shaubert solved this integral in closed form. Their solutions for the E-plane ($E_\theta^i(\theta)$) and H-plane ($E_\theta^i(\phi)$) are: [16]

$$E_\theta^i(\theta) = E_a^i\left(k_o w^i cos\theta\right)\sqrt{\frac{2}{sin\theta}}\left(e^{-jk_o c^i{}_L}\frac{F^*\left(u_h^i\right)-F^*\left(u_l^i\right)}{\sqrt{c^i-sin\theta}} + \Gamma e^{jk_o c^i{}_L}\frac{F\left(u_h^{-i}\right)-F\left(u_l^{-i}\right)}{\sqrt{c^i+sin\theta}}\right) \quad (25)$$

$$\begin{aligned} E_\theta^i(\phi) = E_a^i(0)\,\langle & \frac{e^{-jk_o c^i{}_L}}{c^i+cos\phi}\left\{sin\phi\left[F\left(p_h^i\right)e^{jv_h^i} - F\left(p_l^i\right)e^{jv_l^i}\right]\right. \\ & \left. + sin\left(\frac{\phi}{2}\right)\sqrt{2(c^i-1)}\left[F^*\left(q_h^i\right) - F^*\left(q_l^i\right)\right]\right\} \\ & - \Gamma\frac{e^{jk_o c^i{}_L}}{c^i-cos\phi}\left\{sin\phi\left[F\left(p_h^i\right)e^{-jv_h^{-i}} - F\left(p_l^i\right)e^{-jv_l^{-i}}\right]\right. \\ & \left. - sin\left(\frac{\phi}{2}\right)\sqrt{2(c^i+1)}\left[F\left(q_h^{-i}\right) - F\left(q_l^{-i}\right)\right]\right\}\rangle \end{aligned} \quad (26)$$

The various substitutions involved with these equations are summarized below:

$$c_i = (\lambda_o/\lambda')_{ith\ section} \quad (27)$$

$$k_o = \frac{2\pi}{\lambda_o} \quad (28)$$

$$u_{h,l}^i = k_o x_{h,l}^i\left(c^i - sin\theta\right) \quad (29)$$

$$u_{h,l}^{-i} = k_o x_{h,l}^i\left(c^i + sin\theta\right) \quad (30)$$

$$v_{h,l}^i = k_o x_{h,l}^i\left(c^i + cos\phi\right) \quad (31)$$

$$v_{h,l}^{-i} = k_o x_{h,l}^i\left(c^i - cos\phi\right) \quad (32)$$

$$q_{h,l}^i = k_o x_{h,l}^i\left(c^i - 1\right) \quad (33)$$

$$q_{h,l}^{-i} = k_o x_{h,l}^i \left(c^i + 1\right) \tag{34}$$

$$p_{h,l}^i = k_o x_{h,l}^i (1 + cos\phi) \tag{35}$$

This formulation has two shortcomings that will prevent its use in the infrared regıon. First, it ignores the effects of a thick film (region 2) on a large-dielectric-constant substrate (region 3). At this time, there is no known method for meeting the effective thickness requirements at infrared frequencies, so this analytical solution may not match our measured results. Secondly, the boundary conditions assume that the metals are perfect electric conductors. At terahertz frequencies, metals develop larger absorption and greater dispersion [17], so this assumption may not be applicable to our formulation. Chapter 3 presents a finite-element-analysis alternative to developing an analytical formulation for the infrared.

1.4 Effects of Parameters

The results above do not readily lend themselves to parametric studies. However, the effects of several antenna parameters have been experimentally observed and can be discussed qualitatively [18-24]. While these effects have been observed at millimeter wave frequencies, we assume that they are applicable in the infrared spectrum. This assumption will require validation through additional testing as described in Chapter 5.

The most important parameter noted by microwave researchers is the effective dielectric thickness. The effective thickness is defined as:

$$t_{eff} = \sqrt{\epsilon_r - 1}\, t_o \tag{36}$$

The allowable range for this parameter is $0.005\lambda_o < t_{eff} < 0.03\ \lambda_o$ [8, 25]. If the effective thickness is too large, additional modes will propagate in the substrate that will destroy the symmetry

between the E- and H-plane radiation patterns. These modes will also negate the assumption that these antennas are transformers of only the TE mode**.** If the effective thickness is too thin, the thin film will not confine the radiation. At terahertz frequencies, the challenge is creating an effective thickness that is thin enough to meet this requirement. The effective thickness has been reportedly reduced by mechanical and photonic methods, such as cutting stubs into the antenna's taper [20], and by placing plasmonic waveguides on the opposite side of the substrate [21]. Other methods include machining holes into the substrate [9], etching the substrate away [22], and using very low dielectric constant materials [9]. These approaches have not yet been attempted in the infrared.

Another parameter of note is the length of the taper. If the length is on the order of a single wavelength, the antenna acts as a resonant antenna [3,8]. The reason for this is the edge of the TSA begins to resemble a dipole antenna with drastic changes to impedance and slotline wavelength in the aperture. The results of dipole behavior are a drastically decreased bandwidth and loss of 3-D symmetry of the farfield radiation pattern.

The next parameter is the width of the aperture. The wider the aperture, the wider the beam pattern in the far field will be [3,8,16]. However, if the aperture is less than one half of a wavelength, the TSA will act as a slotline antenna, which is not very efficient [25-28]. Also important to the radiation pattern is the overall width of the antenna; the metal edges next to the aperture will allow currents and thus will affect the far-field pattern. The effect is more noticeable in the E-plane than in the H-plane, and thus this parameter can be used to affect the three-dimensional symmetry of the radiation pattern [8].

The geometry of the terminating slotline will have effects on the entire assembly. If the slotline is too narrow, the slotline will act as a plasmonic waveguide. Thus, the propagation distance will increase, but the confinement (and thus the power density at the diode) will suffer [25-28]. Additionally, the impedance of the system tends to match the impedance of the terminating slotline. The slotline can thus be used to fine-tune the bandwidth of the antenna. A method of adjusting this impedance currently under investigation is the addition of a stub that expands the slotline for a short distance [10]. Numerical models show that the stub dimensions will slightly affect both the resistance and the reactivity (ie, the real and imaginary components of the impedance) of the antenna.

1.5 Tapered Slot Antenna Fabrication

The critical dimensions of a TSA operating in the infrared are tens of microns in size, without taking the MOM diode into account. Conventional photolithography would support these dimensions; however, the diode requires exposure dimensions of approximately 100 nm by 100 nm. Because the diode will be integrated directly into the antenna, electron-beam lithography is used for all structures. A single-side polished crystaline silicon wafer is used to structurally support the components. To electrically isolate the diode, it is placed on an insulator, normally deposited onto the wafer by spin coating. The insulator is capped with two electron beam resists: 450 nm of methyl methacrylate (MMA) beneath 70 nm of polymethyl methacrylate (PMMA). Two resists are required for the construction of the MOM diode, as discussed in Chapter 2.

Because the TSA is an endfire antenna, the edge of the antenna should coincide with the edge of the wafer. To accomplish this, the wafer, insulating thin film, and resists are cleaved

along the wafer's crystalline axis. This creates an edge that is theoretically atomically straight. The antenna pattern will be written up to and across the edge, so any edge variance less than a few microns is acceptable. The wafer must be cleaved after the insulator layer and the electron-beam resists are applied, to prevent an edge bead from forming.

The device design is created using the Tanner EDA L-Edit CAD program. The pattern is programmed onto the Vistec EBPG5000+ Electron Beam Lithography system, and the pattern is aligned such that the design overlaps the cleaved edge of the wafer. In order to minimize errors caused by multiple exposures, the entire pattern is written at one time. The electrical leads are written with a 100 nA beam with a spot size of approximately 96 nm. Diode patterns are written with a 1 nA beam with a beam spot size of approximately 10 nm. To prevent over-development of the resist, the antenna is written at as low a dose as possible (200-300 $\mu C/cm^2$). A second thin (250 nm wide) pattern traces the internal antenna edges and the diode to ensure sharp features in the resist. This second pattern's beam typically operates with a 5 nm step size at 300 $\mu C/cm^2$. These exposures are discussed in greater detail in Chapter 2.

The wafer is placed in 3:1 isopropanol:methyl isobutyl ketone (IPA:MIBK) developer for 60 seconds to remove the exposed resist, rinsed in IPA and placed in an O_2 plasma to remove any residual exposed resist. Metal is then deposited onto the entire wafer surface using a AJA International high vacuum electron-beam evaporator. The choice of metal used is based on the diode's design. Fig. 5 shows the fabrication process. Fig. 6 shows the completed antenna; note that this scanning electron microscope image is not an actual final antenna, as the pictured antenna was built in the center of the wafer instead of the edge. Also, this SEM image was taken before lift off, so the resist on the outside of the antenna and the inner taper region still exists.

The dashed line shows where the wafer edge would be if this had been written across a cleaved edge.

The final construction step is to remove the remaining resist and all of the metal deposited on it, a process known as lift-off. It is accomplished by immersing the wafer in methylene chloride.

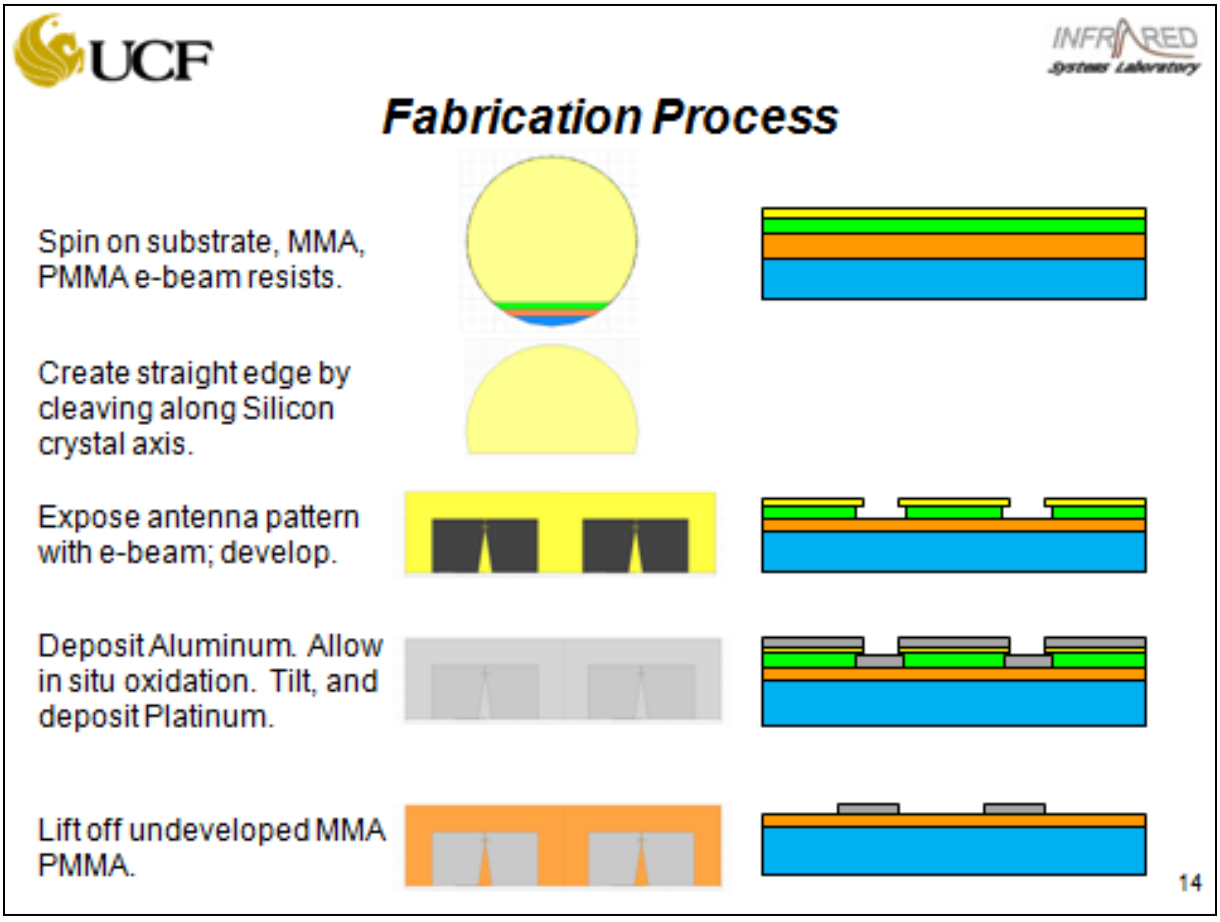

Figure 5. Schematic of antenna fabrication. Yellow represents the PMMA, green is MMA, orange is BCB, and blue is the silicon wafer. Grey represents the metals.

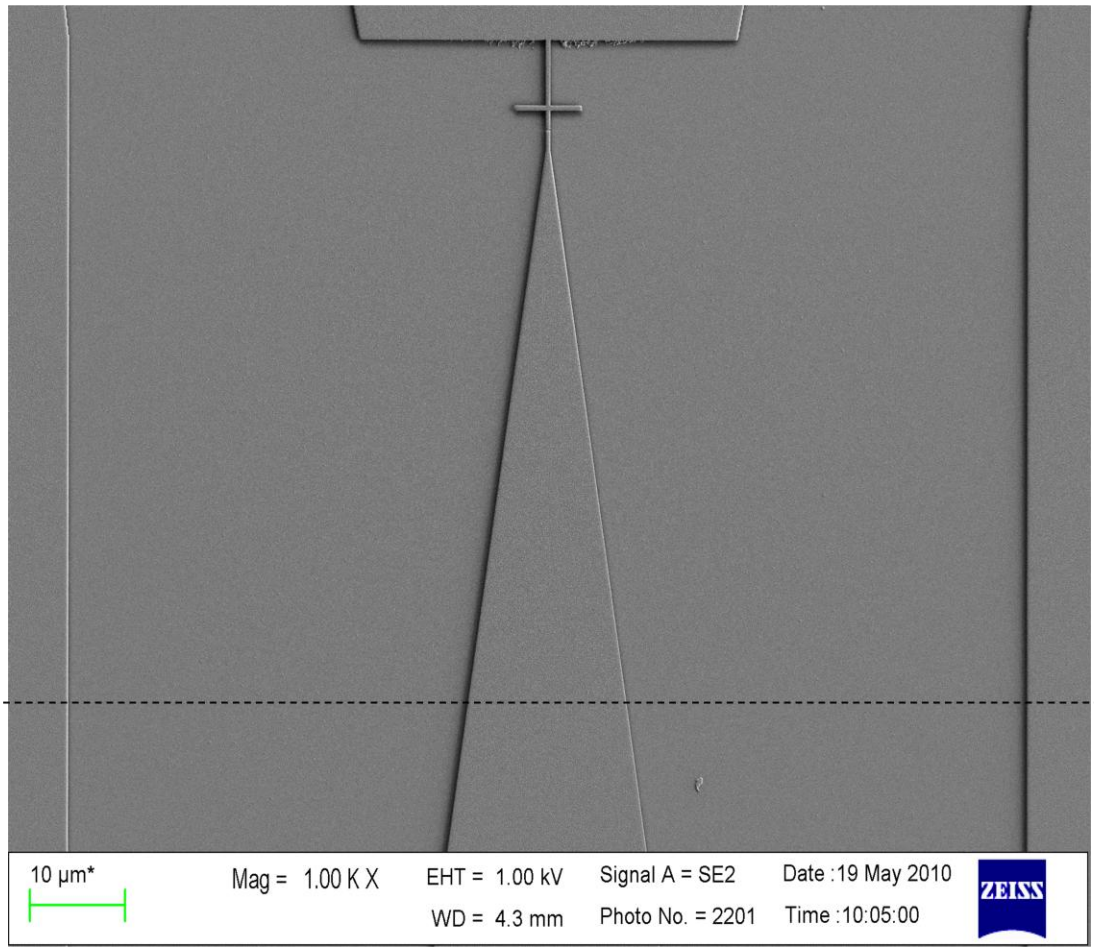

Figure 6. Scanning electron microscope image of the resist of an infrared LTSA. Note that the dashed line represents where the cleaved edge of the wafer would be.

CHAPTER TWO: ANTENNA-COUPLED MOM DIODES

2.1 Metal-Oxide-Metal Tunnel Diodes

Once the field is confined by the antenna, it can be detected. A novel method of detecting a signal is to integrate a metal – oxide – metal (MOM) diode into the slotline. The use of these diodes with dipole antennas to detect infrared radiation has been well studied by Bean, et al. [29-36]. It is possible to integrate the diode directly onto a tapered slot antenna, as discussed in Chapter 1.

The MOM diode operates in the infrared region of the spectrum as a current rectifier. An asymmetric MOM diode is created by separating two metals of different work functions with a thin (a few nanometers) insulator. In this case an oxide layer serves as the insulator, as shown in Fig. 7. The insulator acts as a barrier to electron movement; however, an internal field is induced because the metals have different work functions. When the diode is exposed to infrared radiation, the incident electric field will modulate the field present in the barrier sufficiently so as to allow preferential electron tunneling events in one direction [30]. This current can be detected using standard low-frequency electrical test equipment, thus making the diode a detector. Because the barrier modulation (and thus the current) varies with the power density of the incident radiation, it is known as a square law detector [31].

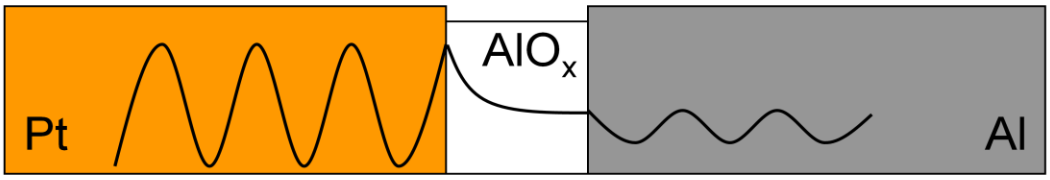

Figure 7. Al/AlOx/Pt diode operation. The thin AlOx layer acts as a potential barrier which an electron can tunnel through. The dark line represents the probability distribution of an electron.

Another factor that must be addressed is the physical size of the diode. For the antenna to react to infrared radiation, its cutoff frequency must be equal to or higher than the desired detection frequency. Its cutoff frequency is a combination of the impedance of the antenna and the diode, which can be modeled as a voltage-dependent resistor in parallel with a capacitor [30]. The cutoff frequency for the circuit, then, is

$$f_c = \frac{1}{2\pi RC} \tag{37}$$

where R is the aggregate resistance of the circuit and C is the capacitance of the diode. The one factor that can be modified is the capacitance, which is defined by

$$C = \frac{\epsilon_{ox}\epsilon_o A}{d} \tag{38}$$

Here, the area A is the one factor that can be engineered. The thickness d must remain small (several nanometers) to allow tunneling, and the dielectric constants are functions of the materials [32]. Therefore, when constructing the diodes, they must have the smallest metal overlap area possible while still maintaining fabrication integrity. The process to create the diodes is discussed at length below. The D* values for these MOM diodes in the infrared have been reported as high as 10^7 Jones. [35]

The diode is formed by depositing a metal, allowing it to create a native oxide layer, and then depositing a second metal with a small offset [31]. This process is known as shadow evaporation, and is illustrated in Fig. 8 [29]. The metals used for the TSA are aluminum (which readily forms an oxide) and platinum, creating the $Al/AlO_x/Pt$ diode.

Because the thick MMA layer of resist is more sensitive, and thus develops more readily than the thin PMMA layer, an undercut will be created beneath the edges of PMMA. If the edges of the features are close enough together, the underlying MMA can be developed away, leaving the PMMA intact to act as a bridge. For this to occur, the pattern edges must be 70-100 nm apart, with the exact distance depending on the resist thickness, sensitivity, and effective electron beam dosage in the region. Fig. 9 shows the completed bridge after development of the resists.

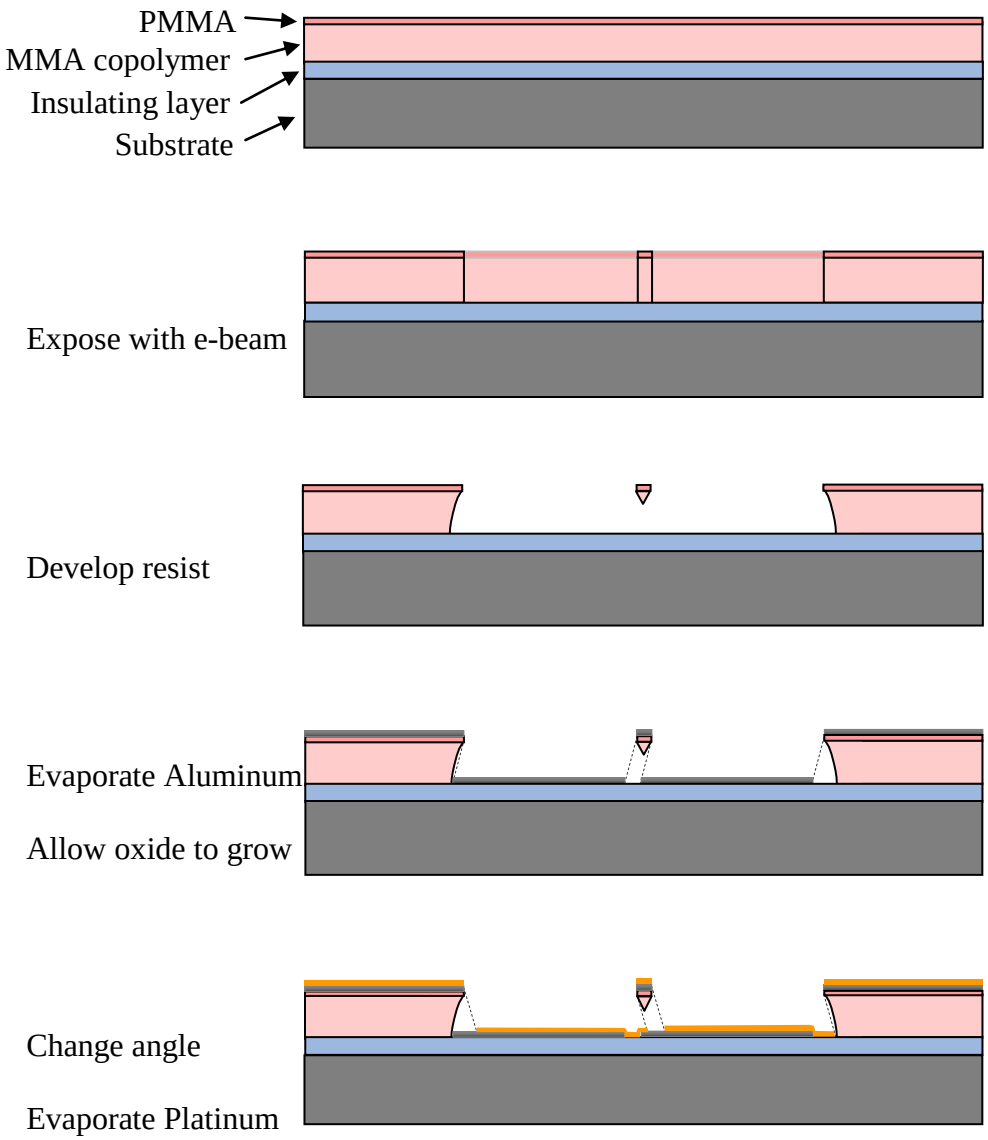

Figure 8. Diode construction schematic. Notice in the third panel ("develop resist") that the undercut of the MMA has formed a PMMA bridge. This bridge then creates shadow areas when aluminum and platinum are deposited at opposing angles (fourth and fifth panels)

The PMMA bridge will create a shadow region on the substrate which will not be coated by the aluminum evaporation. See Fig. 8. This is due to the inherent directional deposition using electron beam evaporation. If the sample tilt is 0° when aligned with the evaporant's path, the stage is tilted to + 7°, and aluminum is deposited. Once the aluminum has been oxidized in a controlled manner, the wafer is tilted to -7° so that the platinum can be deposited to complete the diode. The only path for electrons to move from one side of the antenna to the other is through the oxide at the diode. When connected to measuring equipment and illuminated with radiation, any fluctuation in signal must be caused by the radiation power modulating the diode's tunneling capability.

For the infrared antenna, a 30-nm layer of aluminum is deposited. The aluminum is then exposed to 100 mTorr of oxygen for 25 minutes. This creates an aluminum oxide layer 2-6 nm thick. The wafer is tilted *in situ* by means of a levered stage, and then a 30-nm layer of platinum is deposited. Because the entire process occurs *in situ*, this process creates an antenna with a diode without the requirements for lithographic alignment or for removal of native oxides.

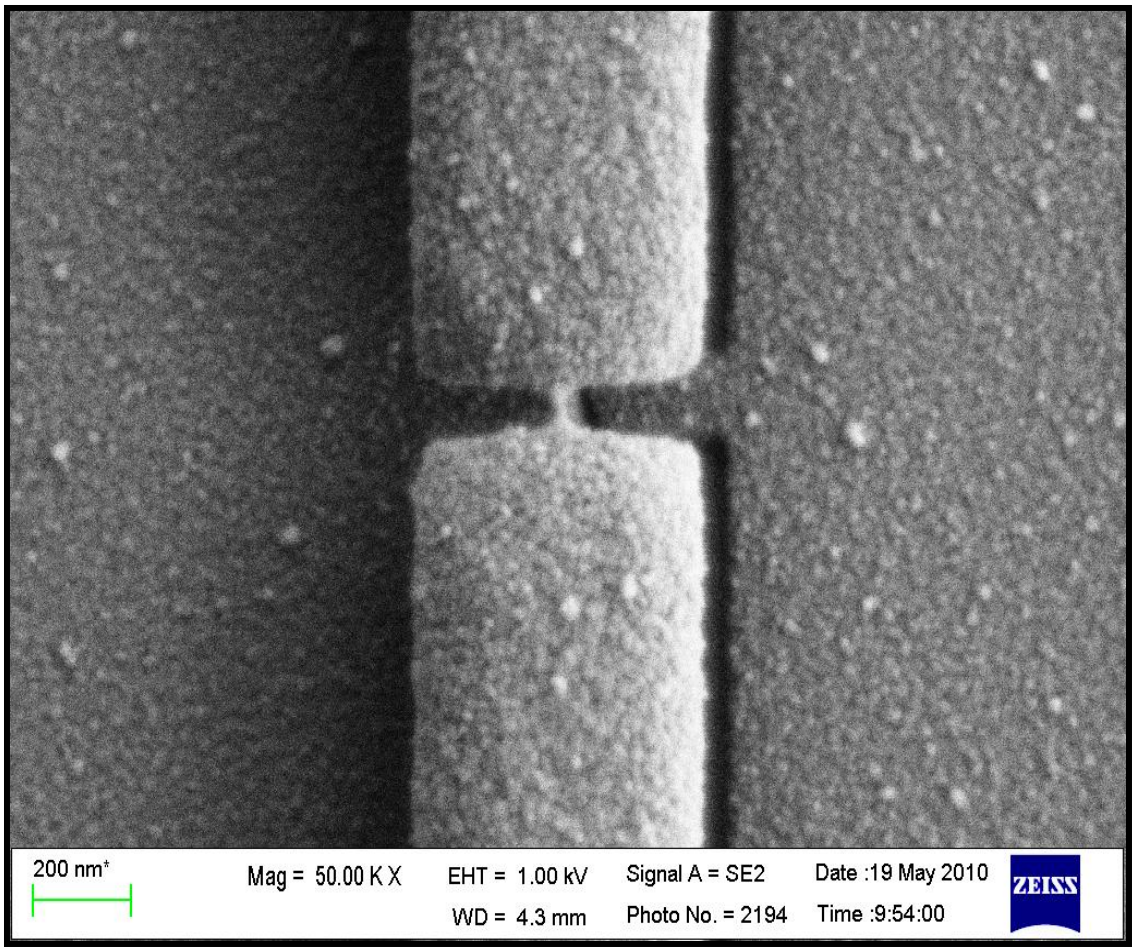

Figure 9. Scanning Electron Microscope image of PMMA Bridge. The bright region is the PMMA elevated above the antenna. The thin portion in the center is the bridge which will allow the diode to be created by shadow evaporation.

Because of the extremely small dimensions of the diode in the antennas, one cannot verify its functionality through microscopic inspection. Instead, the device is connected to a HP4145B semiconductor parameter analyzer using electric probes. The analyzer applies a small voltage (less than 0.5 volts) across the diode and measures the resulting current. By sweeping the voltage, an I-V curve is generated. The diode should have a non-linear I-V relationship; the magnitude of the non-linearity determines its responsivity when subjected to infrared radiation.

2.2 MOM Diode Impact on Fabrication

The ability to consistently create functioning diodes is essential to the study of radiation patterns of the infrared TSA. Several months of effort went into building the TSA device shown in Fig. 6 (Chapter 1). There appeared two modes of failure for these devices. The failure modes proved too difficult to overcome with adequate device yield, and new fabrication methods were developed. Eventually, the failures led to a new antenna design.

The first failure mode was the breaking of the bridge, either during development or during the metal deposition. Because of the dosing required for the large metal planes, backscattered electrons affected the PMMA bridge resist. This had the effect of weakening the bridge so that it would fail in development (Fig. 10) or when metal was applied. This would result in a short circuit, as there would be no electrical path that forced the current to pass through the high resistance oxide of the diode.

The solution to this was to lower the dose of the antenna bodies. Recent developments in electron beam lithography have led to the development of proximity effect correction (PEC) software, which improves on standard lithography by accounting for the backscatter of electrons and calculating the reduced initial dose required. Working with Dr. Jeff Bean at the Georgia Tech Research Institute, we used PEC software to develop a dosing arrangement that would limit the number of backscattered electrons into the PMMA bridge region (Fig. 11). By adapting this dosing scheme, we succeeded in creating bridges that survived the development and deposition processes.

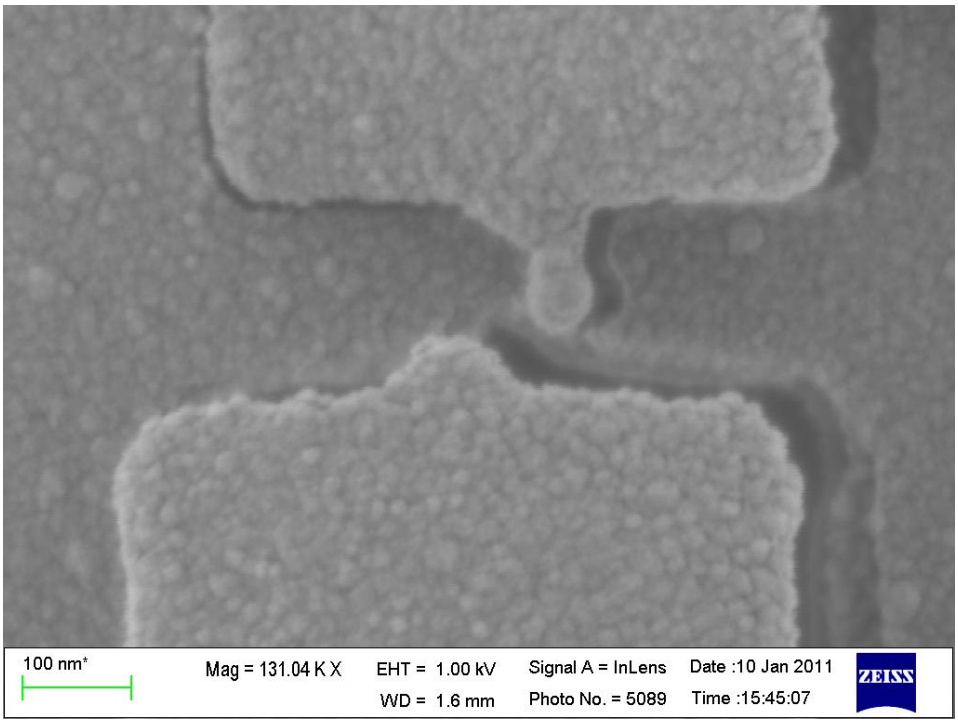

Figure 10. Broken resist bridge caused by overdosing.

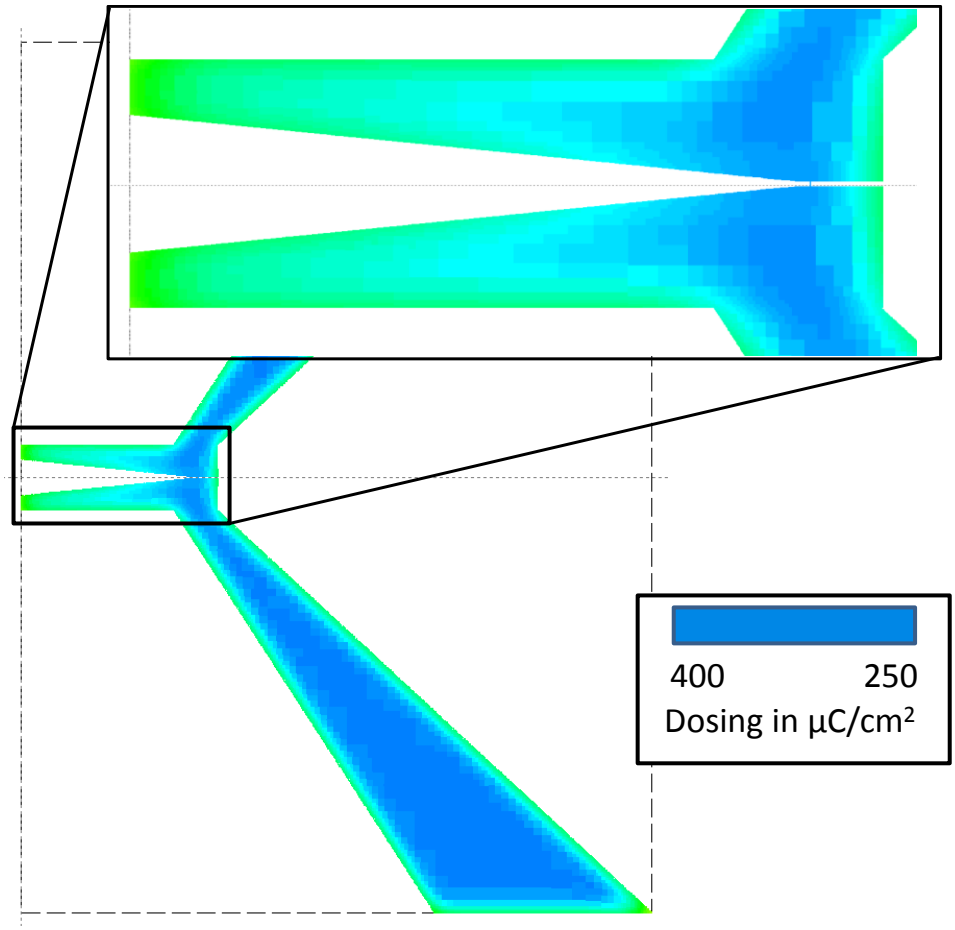

Figure 11. Recommended dosing of the TSA to prevent overdosing of bridge region.

The second failure mode was a breaking of electrical contact in the diode itself after metal deposition, which results in an open circuit. Fig. 12 is an micrograph of a functioning diode ruined by a crack that formed along the slot after the metal deposition. This same failure mode was noticed in several diodes, leading to the realization that the electrical connections were being pulled apart. As the evaporated metals cooled from their vapor, they contract slightly. The force of this contraction on the BCB thin film surface is proportional to the width of the metal plane. In a thin line, this pulling is not enough to break the diodes. However, the metal

planes of the TSA are tens of microns across. This tensile force caused the top surface of the BCB to fail, resulting in the cracks seen in Fig.s 12 and 13.

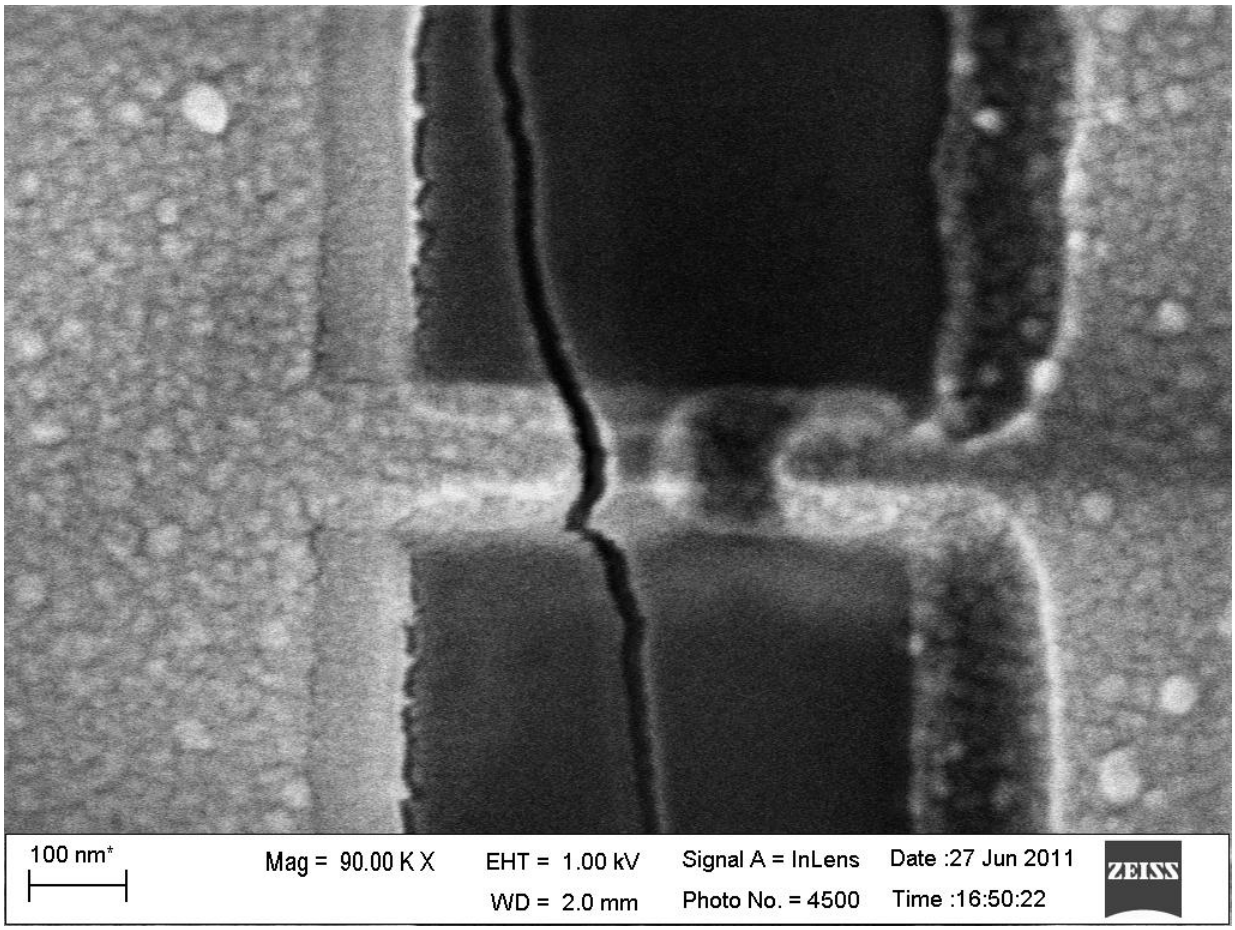

Figure 12. Broken electrical connection near the diode.

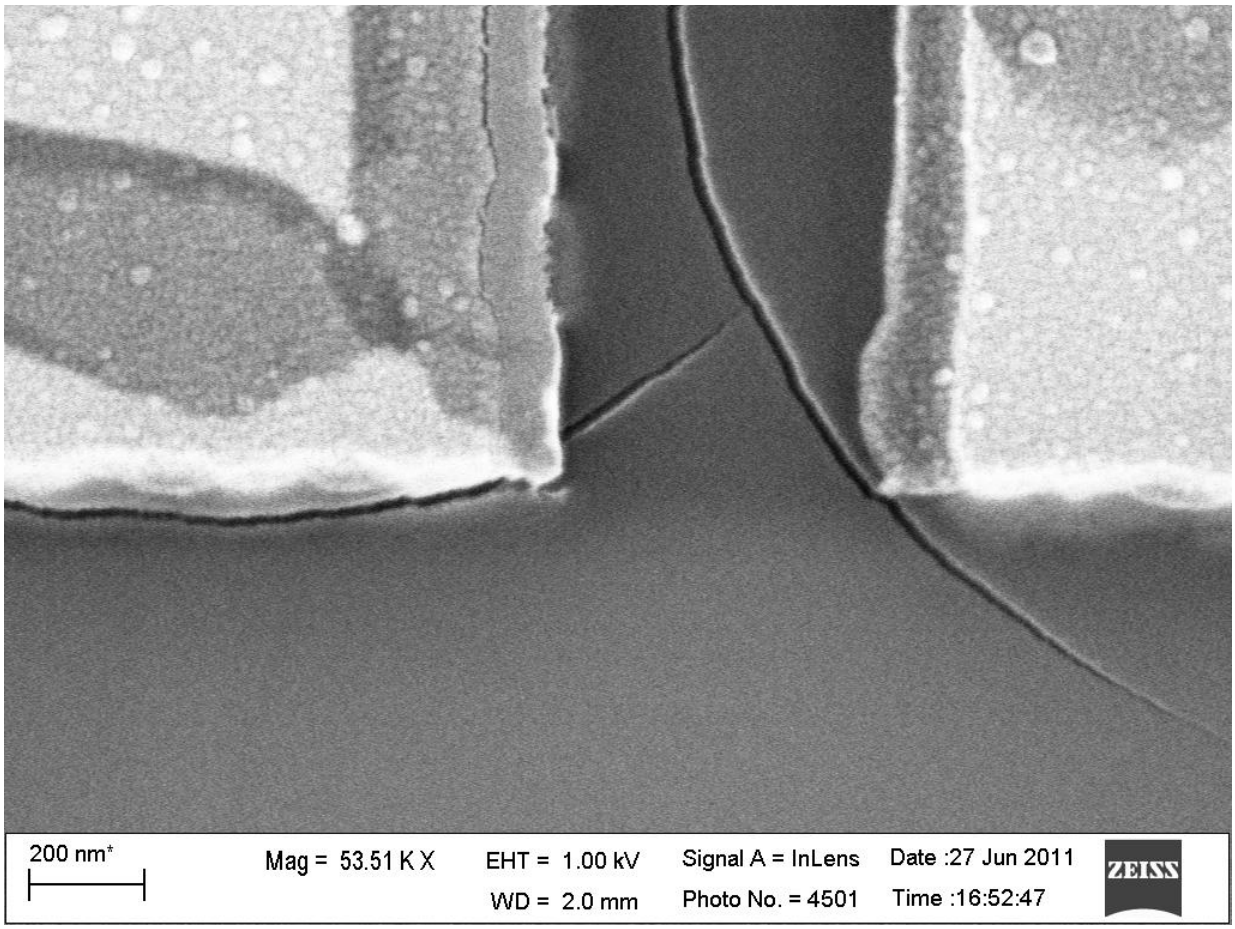

Figure 13. Cracks in the BCB at the entrance to the slot away from the taper.

2.3 A New Antenna Design: The V-LTSA

We developed two solutions to prevent this mode of failure. First, we could change the thin film from polymer BCB to crystalline zinc sulfide. Ideally this crystalline structure would withstand the tensile forces caused by the cooling metal. However, we discovered that zinc sulfide's poor adhesion properties would allow for metal failure when placed into the laser (Fig.14). Though this problem was later solved by using a chromium adhesion layer, at the time, this failure mode caused us to find another solution.

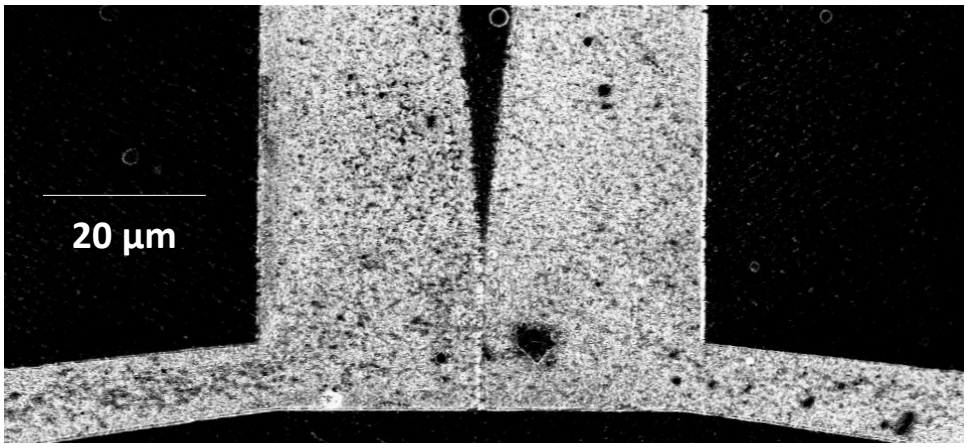

Figure 14. Material failure of device on ZnS after exposure to laser. The aluminum and platinum have detached locally from the ZnS, causing the texture seen here.

The solution was to mimic the successes of other diode geometries. Others have successfully integrated the MOM diode into coplanar striplines (CPS), as in Fig. 15. [34] These striplines have the advantage of having a much smaller width (200 nm) than the metal plates, which reduces the tensile force. Additionally, others have built TSAs that feed CPS structures instead of slotline structures [45] so we know that they can be fabricated and tested (Fig. 15). Thus, in order to prevent cracking in the BCB thin film, we developed the infrared V-shaped linear tapered slot antenna (V-LTSA), shown in Fig. 16. We achieve a success rate over 70% of working diodes with this new geometry. With this new design, we were able to begin modeling, fabricating and testing these devices.

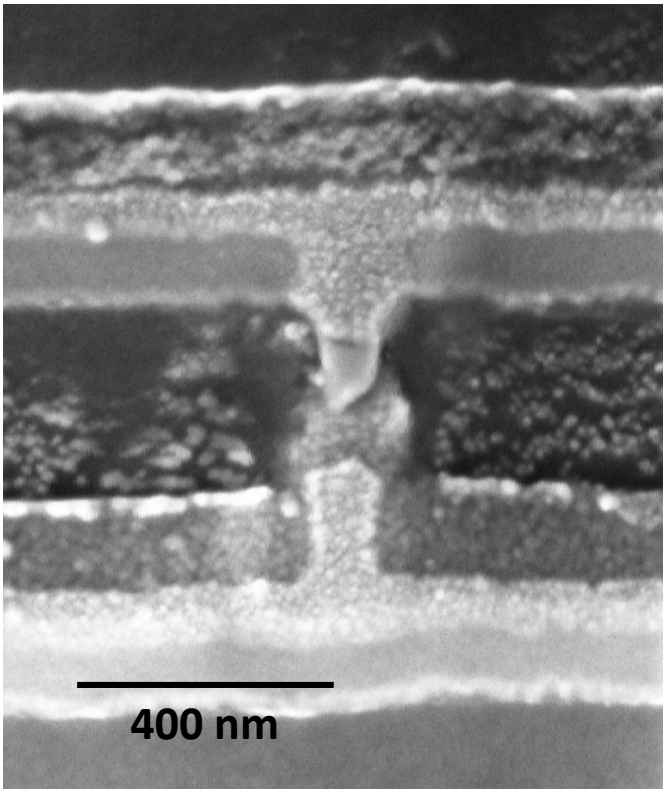

Figure 15. Operational diode in a coplanar stripline

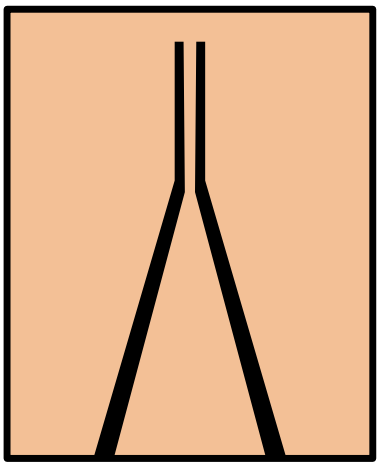

Figure 16. The V-LTSA concept.

CHAPTER THREE: ELECTROMAGNETIC FIELD SIMULATIONS

3.1 Ansoft HFSS

The costs in time, equipment and materials required to create the TSA devices are fairly high. Without an analytical solution that has been proven at infrared frequencies, the effects of numerous parameters must be tested, meaning multiple devices must be fabricated and tested. An ideal method to conduct these tests is accurate modeling using Ansoft's High Frequency Structure Simulator (HFSS) [37].

HFSS allows the user to build a structure with variable dimensions and properties. Additionally, it allows a variety of materials to be modeled. Another key feature allows the user to define the frequency and physical parameters of the excitation radiation. Thus, HFSS allows a TSA to be modeled exactly as built beforehand. The actual testing of the device is still required to validate the HFSS results, but the effects of parametric changes can be accurately forecast without time consuming, iterative device construction. This agreement between model and device is critical in the absence of an analytical solution. Without the model, there would be no standard with which to compare the device's response.

The underlying construct of the modeling software is the development of a three-dimensional mesh that accurately models the material properties of the components. This mesh is then subjected to electromagnetic radiation, and the electric and magnetic fields are mathematically propagated from point to point through the mesh. Then, in areas of high field concentration, the mesh is refined to be denser and the fields are propagated again. This takes place until the solutions for consecutive iterations "converge", meaning that the S11 scattering parameter does not change significantly with changes in the mesh. The result is that the field can

be found at any point within the structure for any given excitation. Therefore, the model has the ability to show where field concentrations exist on the model, and can show if the antenna is operating as a traveling wave antenna. Exact characteristics, such as bandwidth, impedance and beamwidth can be calculated from the model.

The user must complete four steps to create a workable model. First, the device must be built with proper dimensions. HFSS will allow parameter studies, so the dimensions can be variable. Second, material properties (namely, the real part of the dielectric constant and loss tangent, or the bulk conductivity for conductors) must be assigned. Because the device is primarily a thin film stack, bulk material properties are not applicable. The material property libraries available with HFSS generally do not pertain to our materials, and therefore are not used. Instead, all material properties are determined using the J.A. Woollam Infrared Variable-Angle Spectroscopic Ellipsometer (IR-VASE), with the data analysis conducted at CREOL by the Infrared Systems Laboratory personnel.

Once the material properties are known, radiation boundaries must be assigned. The purpose of radiation boundaries is to act as perfect absorbers so as to prevent non-physical reflections from affecting the simulation. These boundaries allow a small model to be built with some surfaces understood to be semi-infinite. For example, on the actual device, radiation that by-passes the antenna will not reflect off an air boundary. Instead it will propagate through the substrate and be attenuated. Instead of building a long substrate (on the order of centimeters) and applying computational models to an enormous mesh, the antenna can be modeled such that radiation bypassing the diode encounters a radiation boundary. That radiation will no longer

affect the simulation. Thus, the antenna can be accurately modeled with a mesh that has total dimensions of tens of microns.

The final step to create a model is to define the excitation radiation. HFSS will allow the radiation to be modeled as a Gaussian beam with a user defined spot size and a user defined zero-phase center. Additionally, the user can define the polarization of the radiation. Another radiation source is a waveport, which launches radiation from the slotline into the antenna. Similarly, a lumped port acts as a radiating dipole in the slotline. These three excitations are discussed below.

3.2 Antenna Modeling Shortcomings

There are two primary shortcoming of the HFSS model that must be addressed. They are the width of the model and the depth of the wafer. By truncating these parameters, one introduces errors into the model that must be considered in the design. Ideally, both dimensions would be several times larger than the spot size of the excitation source to avoid any clipping or edge effects. However, due to computational constraints of HFSS, this is not a practical solution.

The dimensions of the infrared tapered slot antenna model in HFSS are much larger than the wavelength of the radiation. As discussed in chapter 1, the taper should be several wavelengths long. The width of the model is determined by the opening angle of the taper, but in general will be several wavelengths. The largest dimension is that of the wafer, which must somehow be included in the model. The wafer is typically approximately 300 μm thick. Therefore, the model volume will be hundreds of cubic wavelengths and will contain millions of tetrahedrons. With the available computing processor (2.67 GHz processor with 24 GB of RAM), accurate, iterative propagation and mesh refinement calculations will take weeks to

complete. This assumes that the system remains well-behaved; often, HFSS will cause the CPU to lock up, especially for large volume models.

Additional concerns force us to use even more volume for the antennas. HFSS will interpret any edge as step function from the material to vacuum, even if boundary conditions specify that the material does not end. Therefore, all edges must be far enough from the antenna so as to not influence the fields in the device. Although the HFSS manual suggests that these edges be at least a quarter wavelength away from the device, I have found that this is insufficient. See Fig. 17 below. The 5 μm distance (blue line) corresponds with a quarter wavelength separation. This does not match the measured data as well the wider model (10 μm on each side), so the wider model parameter is used.

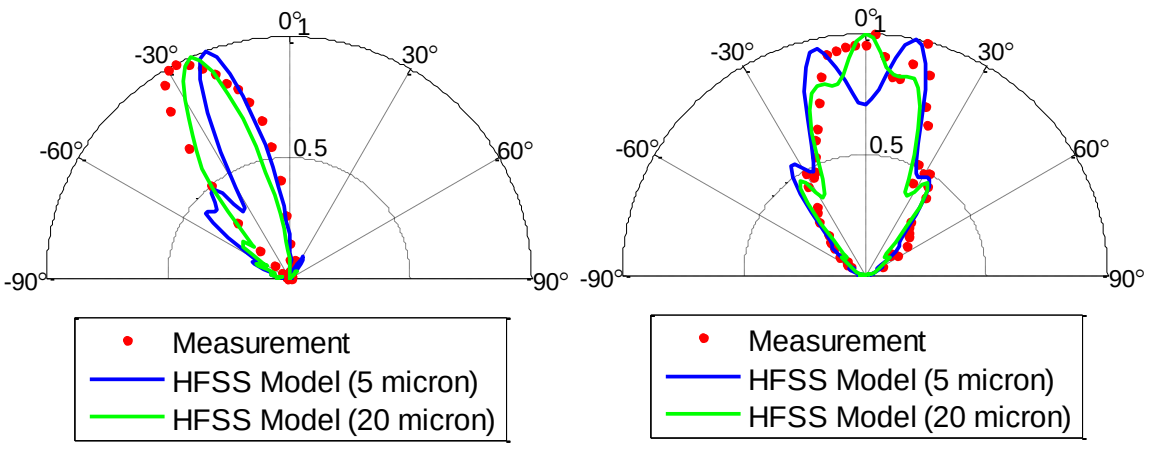

(a) (b)

Figure 17. H-Plane (a) and E-plane (b) far field radiation patterns for different model widths. Distances are total extent of wafer and thin film ouside the antenna included in the HFSS model.

Another difficulty with the model is the far-field prediction. The far-field pattern is calculated by taking the Fourier transform of the field at the surface of the model. Because we

have truncated the depth of the silicon to save processor time, the field along the surface of the silicon will be incomplete. The choice of boundary condition and the depth of the silicon in the model will have to be adjusted so that the far-field pattern accurately predicts the measured data.

In order to save processing time, one can attempt to model the substrate (i.e., silicon wafer) with a thinner structure. In order to accomplish this, one must determine what value of thickness adequately predicts the radiation patterns seen with actual devices. In Fig. 18 we can visualize how the thickness of the silicon affects the radiation patterns. All three solid curves model the measured data fairly well. The 10 μm thickness best models the H-plane data because it does not display any appreciable sidelobes, so it was chosen as the best thickness.

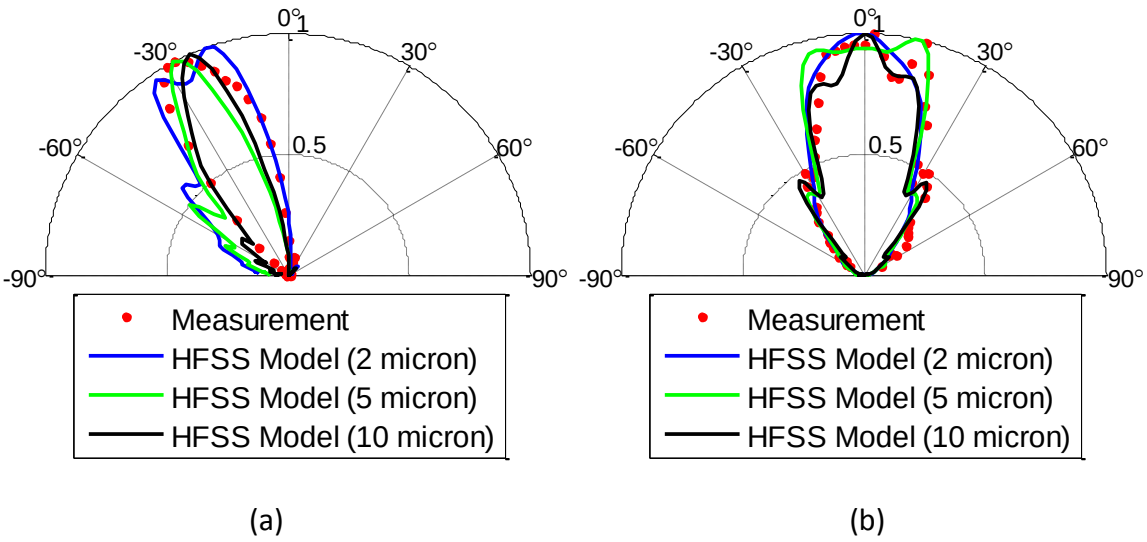

Figure 18. H-Plane (a) and E-plane (b) far field radiation patterns predictions for various thicknesses of the silicon substrate using layered impedance boundary conditions. Distances are the depths of silicon included in the HFSS model.

Finally, there are several boundaries that can be used: radiation, perfectly matched layer (PML), and impedance layers. Again, the best boundary to use is the one that allows the best fit between the model and the measured data. See Fig. 19 for a comparison of the different

boundary types. Based on the H-plane pattern agreement, the layered impedance boundary is used.

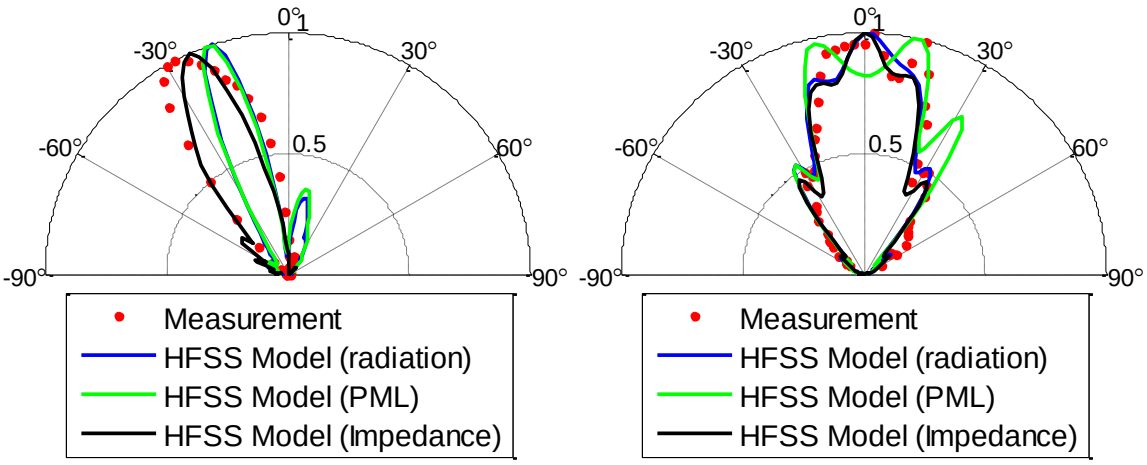

(a) (b)

Figure 19. H-Plane (a) and E-plane (b) far field radiation pattern predictions for three different boundary conditions assuming a 10 µm thick silicon wafer.

The best fit occurs when the silicon is modeled as being 10 µm thick with an "impedance boundary" (see Fig 19, the black line). This boundary calculates the field as if a certain thickness of material were there by assigning it a bulk index of refraction and absorption. Even for a represented thickness of 300 µm, this method does lead to reflections at the impedance- air interface, and so a 5 µm thick silicon layer must be added to the bottom to prevent this reflection. This stack correctly predicts the angle of the maximum signal response in the H-plane.

3.3 Excitation Modeling

There are several excitation methods available in HFSS. Among the applicable methods are the external beam excitation, the lumped port and the waveport. I used each of these three

methods to generate a far-field pattern, and then compared these results with the actual data to determine which offered the best model of the system.

The external beam method allows the user to apply a Gaussian beam of radiation to the antenna, specifying the beam waist location, the spot size, and the direction. The antenna's response can be simulated by placing a model of the MOM diode in the slotline. The response of the actual device will be proportional to the model's calculated dissipated power in the oxide layer of the diode. Therefore, by plotting the dissipated power as a function of angle of incidence, one should be able to accurately simulate the far-field radiation pattern. This method is exactly analogous to the use of an antenna test range (see Chapter 4). However, we noticed several shortcomings with this model. First, the features of the radiation pattern are influenced by minor changes in the coordinates of the beam waist. Because the phase center of the antenna is not analytically known, we do not know the coordinates of the beam waist when the device is tested. Therefore, one must conduct an exhaustive, time-consuming coordinate scan to find a best-fit radiation pattern. This adds three more variables to the model of the antenna, and proves very difficult to validate. An additional drawback is that the resulting radiation pattern is only valid for one variable, either elevation or azimuth. A three-dimensional radiation pattern would require the stitching together of many individual radiation patterns.

The lumped port method places an infinitesimal dipole at the location of the diode. This dipole radiates in all directions, creating the far field radiation pattern of the antenna. The drawback of this method is that the radiation does not remain confined to the slotline because it radiates in all directions. Therefore, it does not adequately model the antenna response because it provides too much radiation out of the plane of the antenna.

The waveport method of excitation provides the most accurate radiation pattern. The waveport element is placed where the diode is actually located. The waveport then excites a mode in the slotline portion of the device. This mode then propagates outward to the tapered slot, and creates the electric and magnetic fields throughout the model volume. The far-field values can be calculated and then squared to provide a three dimensional radiation intensity pattern. Because the diode is a square-law detector, its response corresponds to the intensity. Therefore, the waveport is exactly analogous to a diode that is transmitting. The transmitted radiation pattern is the same as the received radiation pattern because of the principle of reciprocity.

CHAPTER FOUR: RADIATION PATTERN MEASUREMENT TECHNIQUES

4.1 . Test Range Equipment

An antenna has several figures of merit that describe its capabilities. The two properties that we use are the angular spread of the radiation pattern (for both E- and H- plane) and the polarization rejection. In order to measure these properties, we require the ability to rotate the antenna about its phase center and the ability to vary the polarization of the incident radation.

Once the diode has been electrically tested using I-V characteristics (chapter 2), it must be electrically connected to measurement equipment. To do this, the silicon wafer portion of the device is taped to a plastic block. This block is then taped to a chip carrier such that the antenna has its endfire direction normal to the chip carrier's surface (see Fig. 20). Gold wire with a 2 mil gauge is connected to the chip carrier output arms and to one side of the antenna using silver paint. The device is then placed into a goniometer with electrical readouts as shown in Fig. 21. The electrical readouts are connected to a 10X current-to-voltage amplifier, then to a lock-in amplifier. This lock-in amplifier receives its frequency synchronization from a chopper wheel which modulates the signal laser. See Figs. 22 and 23 for schematics of the entire system.

The radiation source is a 1 W CO_2 laser operating at 10.6 μm. Neutral density filters are used to prevent damage to optical components. Various lenses are used to deliver the radiation to the antenna in an F/8 cone. A wire grid polarizer defines the polarization of the test light such that it is vertical to the table top. A portion of this light is picked off and sent into a power meter that will allow the antenna's response data to be normalized with respect to the laser's power fluctuations. A half-wave plate allows the linear polarization of the test radiation to be rotated so that any linear polarization can be used. This is important, as one of the characteristics of the

TSA is polarization discrimination. If light is cross-polarized (i.e., polarized perpendicular to the antenna's plane), it will not experience the gain of co–polarized light.

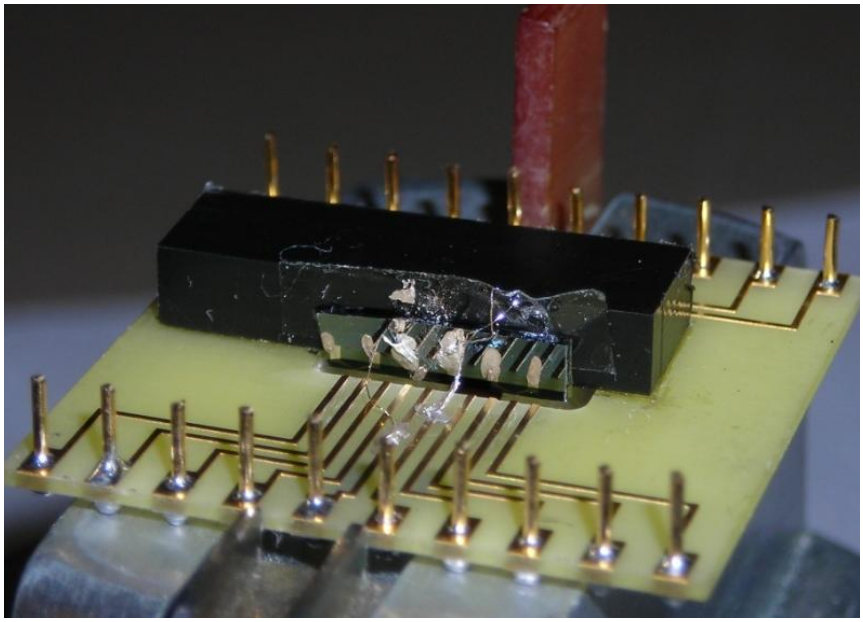

Figure 20. Connecting the devices to the chip carrier with silver paint.

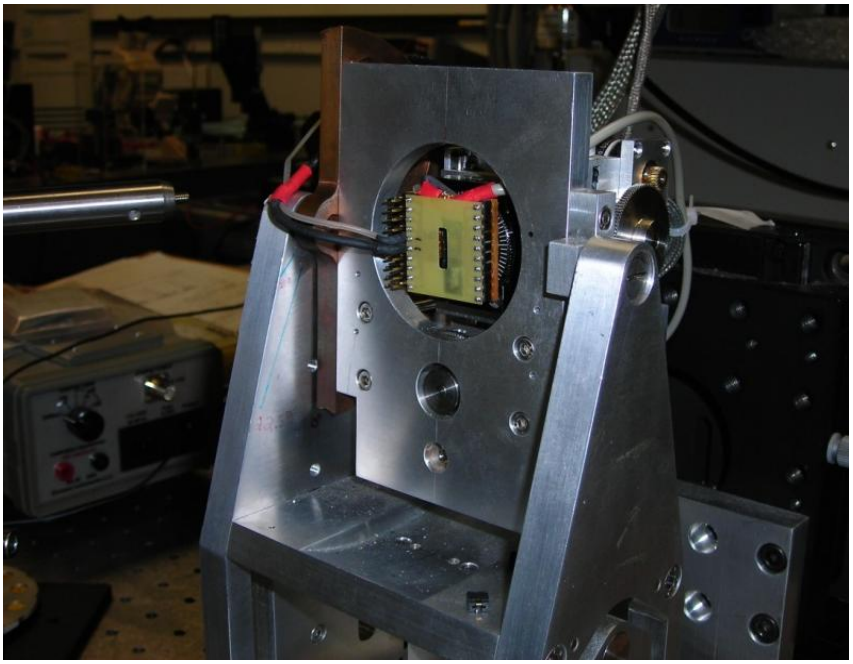

Figure 21. Mechanical and electrical connections to the six-degree of freedom goniometer.

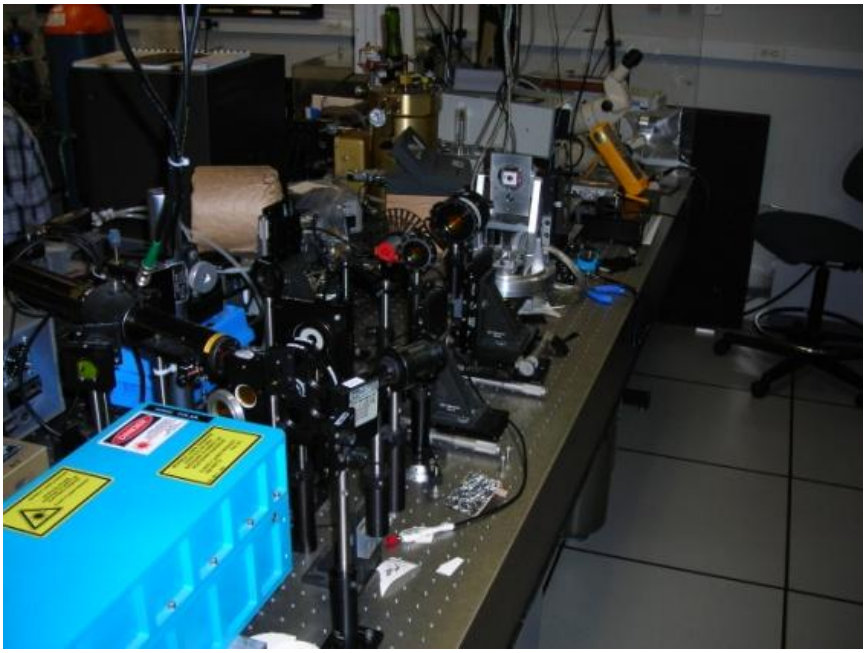

Figure 22. Test set-up for radiation pattern measurements.

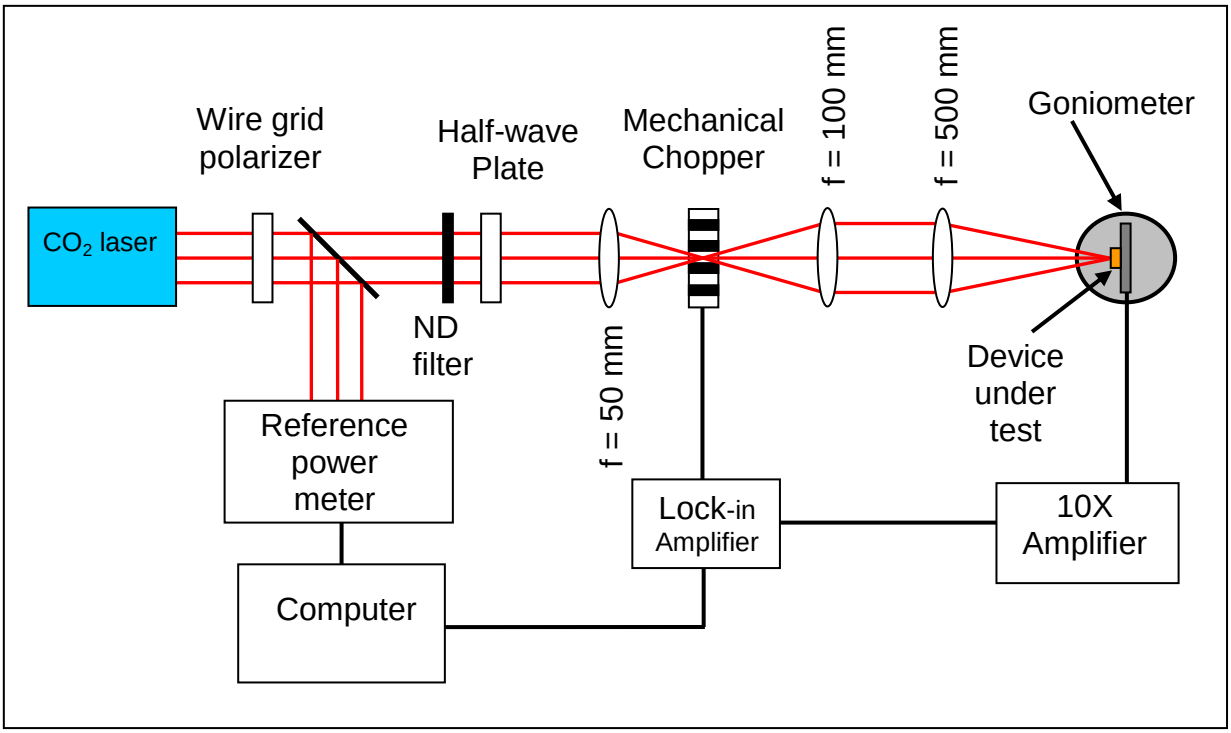

Figure 23. Test set-up schematic for radiation pattern measurements.

4.2 Aligning a device with an off-axis radiation pattern.

The requirement for an antenna test range is to produce a uniform phase and amplitude across the entire aperture under test [39]. There are two methods of measuring an antenna's response in receiving mode. One can either move a signal in a spherical trajectory around a stationary antenna, or one can rotate the antenna through a number of angles around a stationary source. Because we are using a CO_2 laser as the source, we choose the latter method. This requires swiveling the antenna without moving the antenna's phase center with respect to the laser beam. This is no small undertaking, as the spot size of the CO_2 laser at focus is only 115 μm [34].

In order to accomplish this task, we use a six-degree-of-freedom goniometer (Fig.24). These six degrees of freedom are used to align the antenna with the rotation axes of the goniometer. The chip carrier is attached to the current measuring equipment by a split coaxial cable that terminates in two fittings specially designed to attach to the goniometer pin outs. Once the antenna is mounted and connected, the goniometer allows us to adjust the three translational degrees of freedom - the x, y, and z location of the antenna – each with a nominal precision of 6 nm (1000 rotations are equivalent to 6 µm of translation.)

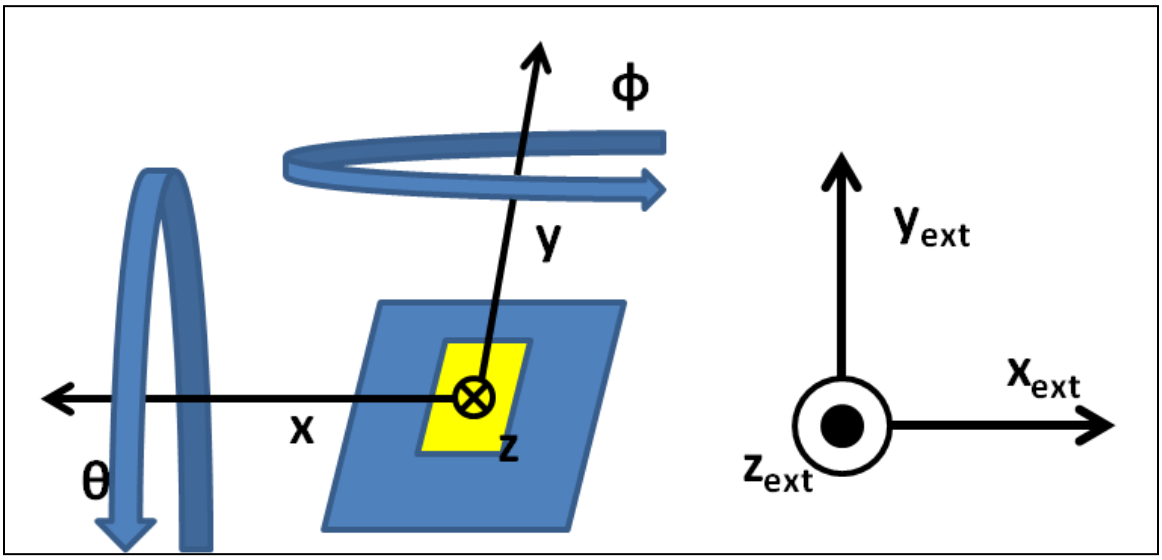

Figure 24. Schematic of the eight axes used in the goniometer. The point of view is from the laser.

Another axis is the azimuth (φ), which is the angle between the y-z plane and the laser beam. Its axis of rotation is parallel to the table's surface normal and the y axis. It has a nominal precision of 0.000052 degrees (19228 rotations per degree). Yet another axis is the elevation (θ), which is the angle between the x-z plane and the laser. Its axis of rotation is parallel to the x axis. It has a nominal precision of 0.000031 degrees (32033 rotations per degree). The sixth axis of rotation allows the sample to spin in the x-y plane with its axis of rotation parallel to the z

axis. It is not automated, and is normally taped to prevent unwanted spinning. This axis defines the TE and TM planes of the antenna, and should be adjusted to have the TSA surface normal parallel to the x axis.

There are three other adjustments that can be made besides these six. They move the entire goniometer in the X-ext, Y-ext, and Z-ext directions. These are useful for aligning the goniometer with the beam waist of the CO2 laser. It is worth noting that these external axes do not necessarily run parallel to the internal directions of the goniometer. They are also not perfectly aligned with the laser beam or the table top. Even with these shortcomings, they will align the goniometer with the laser given an iterative approach.

The alignment process is to co-locate the device's phase center with the rotation axes of the goniometer, then align the center of rotation of the goniometer with the beam waist. The mathematics and procedures for alignment of devices with symmetric radiation patterns, either endfire or broadside, have already been published [38]. However, as discussed in chapter 2, the infrared TSA response is not symmetric in the H-plane. When placed on a BCB/Silicon wafer, the angle of maximum response is about 30° above the plane of the TSA, with the radiation coming from the air side as opposed to the silicon side. The response from endfire is negligible, and the signal from radiation from the silicon substrate is also negligible. Because measurements are not available at positive, negative and zero angles, a new set of equations must be developed to align devices with asymmetric radiation patterns.

We will derive the process for the H-plane, which can be generalized to the E-plane on our system by using the opposite sign for the angles. This use of opposite angles is necessary because of our definition of positive elevation and azimuth on the goniometer. A positive

elevation tilts the y axis toward the laser, but a positive azimuth tilts the positive x axis away from the laser. Changing the sign of the elevation angle in the following calculations will allow for the same mathematics to be used for alignment in both the E-Plane and H-Plane.

The geometry of the problem is shown in Fig. 25. The device is shown as a square, and the center of rotation (in this x-z plane) is shown as a circled x. The laser beam center line is shown as a red line. The variables Δx and Δz are the displacements that the device must move to coincide with the center of rotation of the device. These displacements have units, but will be calculated as a number of rotations of the stepping motors. M_1 and M_2 are the displacements that the antenna must travel to be at the center of the laser beam when the goniometer is tilted to θ_1 and θ_2, respectively. These values can be measured by rotating the goniometer to the desired angle, and then scanning the device in the x direction and finding the location of the maximum signal. Note that if the device was located at the center of rotation, M_1 and M_2 would be zero.

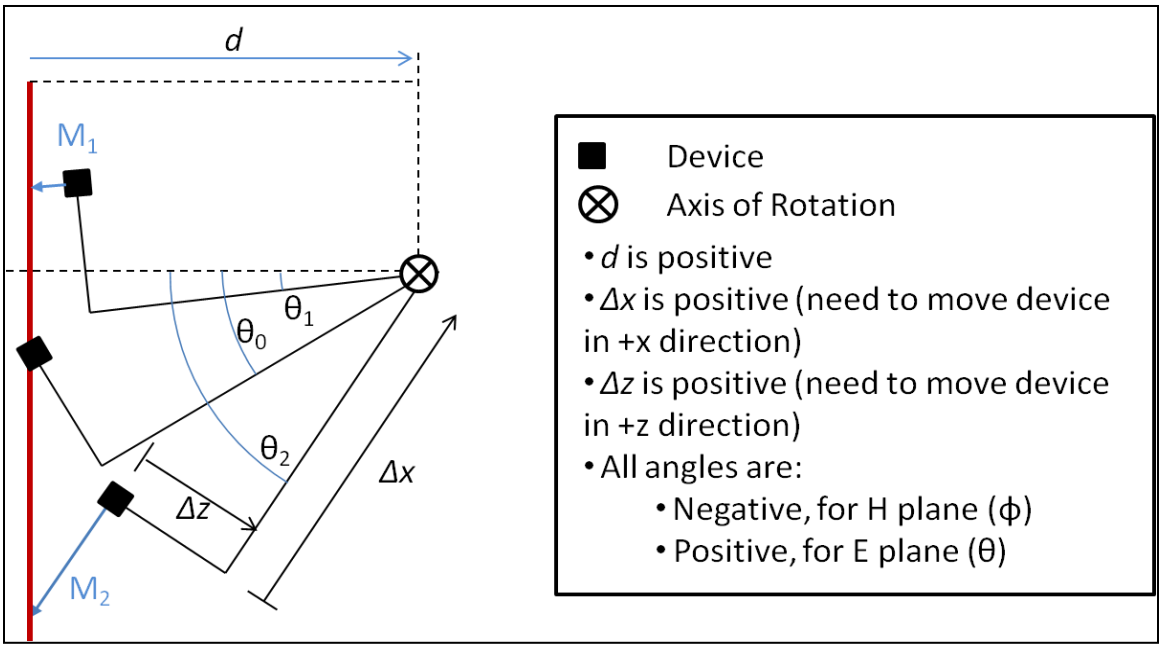

Figure 25. Schematic showing the relevant variables and sign convention for off-broadside alignment procedure

We align the device with the laser at some initial angle, so that $M_0 = 0$. We then move the device to two different angles (θ_1 and θ_2), and measure the displacements M_1 and M_2. We notice from Fig. 25 that the one constant for all three angles is the horizontal distance (d) from the laser beam center to the axis of rotation. For the initial angle (θ_o), this distance is:

$$d = |\Delta x cos\theta_o| + |\Delta z sin\theta_o| \tag{39}$$

For our geometry, sin(θ_o) is a negative value. Therefore,

$$d = \Delta x cos\theta_o - \Delta z sin \tag{40}$$

We then rotate to another angle. The distance (d) from the center of the laser beam to the axis of rotation does not change. We now have to add in the term for M_1, which is negative:

$$d = \Delta x cos\theta_1 - \Delta z sin\theta_1 - M_1 cos\theta_1 \tag{41}$$

It is worth noting that if M_1 were positive, the device would be located to the left of the laser in Fig. 25. In this case, the first two terms in (above) would be greater than d, and the last term

would need to be negative. Thus, this equation is applicable to either positive or negative measurements of M_1. Likewise, for the second angle after the initial angle,

$$d = \Delta x cos\theta_2 - \Delta z sin\theta_2 - M_2 cos\theta_2 \tag{42}$$

This system of equations now has three independent equations and three unknowns (d, Δx and Δz). Substituting (2) into (1),

$$\Delta x cos\theta_o - \Delta z sin\theta_o = \Delta x cos\theta_1 - \Delta z sin\theta_1 - M_1 cos\theta_1 \tag{43}$$

Solving for Δx,

$$\Delta x = \frac{\Delta z(sin\theta_o - sin\theta_1) - M_1 cos\theta_1}{(\cos\theta_o - cos\theta_1)} \tag{44}$$

Using Equations (1) and (3) we can solve for Δz,

$$\Delta z = \frac{\Delta x(cos\theta_2 - cos\theta_o) - M_2 cos\theta_2}{(\sin\theta_2 - sin\theta_0)} \tag{45}$$

Substituting (6) into (5) and solving for Δx,

$$\Delta x = \frac{\frac{\Delta x(cos\theta_2 - cos\theta_o) - M_2 cos\theta_2}{(\sin\theta_2 - sin\theta_0)}(sin\theta_o - sin\theta_1) - M_1 cos\theta_1}{(\cos\theta_o - cos\theta_1)} \tag{46}$$

$$\Delta x = \frac{\frac{M_2 cos\theta_2(sin\theta_o - sin\theta_1)}{(\sin\theta_2 - sin\theta_0)} + M_1 cos\theta_1}{\left[\frac{(cos\theta_2 - cos\theta_o)(sin\theta_o - sin\theta_1)}{(\sin\theta_2 - sin\theta_0)} - (\cos\theta_o - cos\theta_1)\right]} \tag{47}$$

Therefore, by finding values of M_1 and M_2, we can find a value for Δx. This value can then be substituted into (45) to find Δz.

If we assume that the angles are very precise (a good approximation given the precision of the step motors in the micrometers), we can assume that the error in angle results in negligible error toward Δx. We find that the error in the value for Δx depends solely on the error of the two measurements, M_1 and M_2. Therefore, by taking careful measurements of M_1 and M_2, we can obtain Δx to good accuracy.

To test the results of this calculation, we must develop a test case using geometry. Assuming a value of Δx = 15000 and Δz = 10000 at an initial angle of θ_o = -30°, we find that d = 17990. So, at a first angle of θ_1 = -10°, M_1 = -1504. For a second degree of θ_2 = -50°, M_2 = -1070. Any motion-control code that does not return these derived values for Δx and Δz is easily seen to have an error. Several other variations are listed below in Table 1.

Table 1. Calculated results for alignment algorithms.

Δx=15000	Δz=10000		d=15000	
θ_o=0	θ_1= -30	θ_2= +30	M_1= 3453	M_2=-8094
Δx= -15000	Δz= +10000		d= -1500	
θ_o=0	θ_1= -30	θ_2= +30	M_1= 8094	M_2= -3453
Δx= +15000	Δz= -10000		d= 7990.38	
θ_o= -30	θ_1= -10	θ_2= -50	M_1= 5123.09	M_2= -9348.36
Δx= -15000	Δz= +10000		d= -7990.38	
θ_o= -30	θ_1= -10	θ_2= -50	M_1= -5123.09	M_2= 9348.36

4.3 Radiation Pattern Measurement

Upon completion of alignment, a LABVIEW program is utilized to control the goniometer and the lock-in amplifier output. The stage rotates the device to a certain angle with respect to the optical axis, and LABVIEW collects a number of readings from the lock-in amplifier, dividing each reading by the reference power meter reading in order to reduce errors caused by laser output fluctuations. Then, the stage rotates the device to another angle and the process is repeated. The resulting data are the responsivity of the antenna at a series of angles. From this data, the -3dB angles can be determined, allowing characterization of the antenna's beam width and rotational symmetry.

CHAPTER FIVE: INFRARED TAPERED SLOT ANTENNA

5.1 Introduction

Infrared antennas have historically been limited by their detector elements. Fast, small bolometers tend to be low-response devices, requiring high field concentrations for dependable results. [41] Therefore, only planar antennas such as dipoles, spirals, bowties and log-periodics have been incorporated into antenna-coupled sensor devices. [42] With the recent developments in IR microdiodes [33], traveling-wave antenna designs with desirable characteristics such as endfire operation and very wide bandwidth are now feasible.

Tapered Slot Antennas (TSAs) [1, 18, 43] offer several desirable capabilities for detection of infrared radiation over existing microstrip antenna coupled detectors. TSAs are endfire planar antennas that begin with a several-wavelength wide aperture cut into the edge of a metal sheet and gradually narrowed into a wave-guiding slot. The endfire operation and low-profile planar geometry offer a degree of integration flexibility unavailable to non-endfire antennas, such as multi-layer stacking. These antennas have been shown experimentally [44] to have a multi-octave bandwidth because they are non-resonant, and an impedance which does not change drastically along the antenna. [16] Instead, radiation is gradually confined into the slot by the metal surfaces. Potential applications of these devices include infrared detection, directional signal transmission and reception, and energy harvesting.

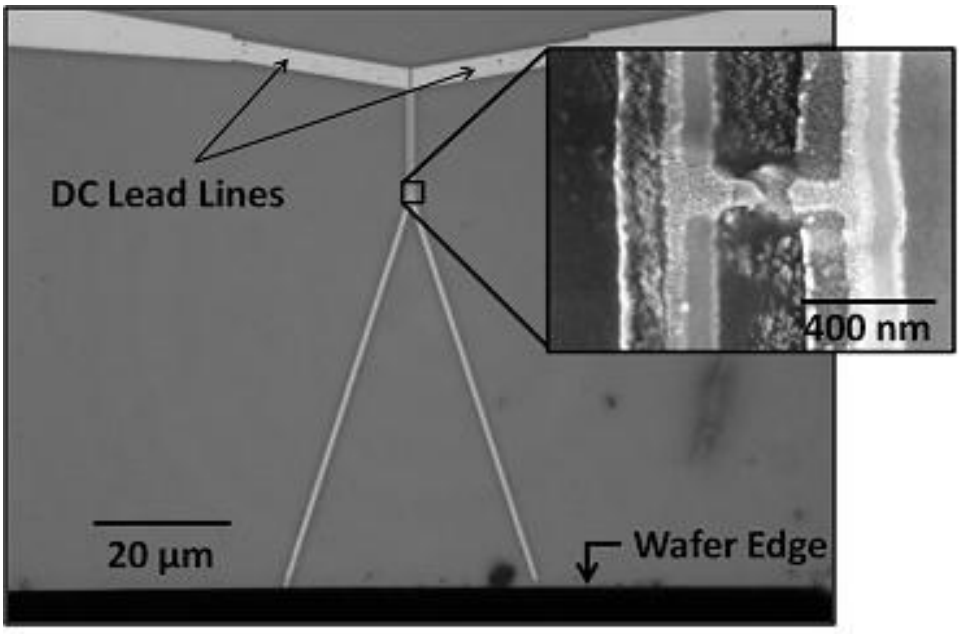

Figure 26. Top view of the device as built with an expanded view of the diode. The bright, smooth metal is platinum, while the darker, coarse metal is aluminum.

In this chapter, we discuss the design, fabrication and characterization of a V-shaped linear TSA (V-LTSA) [45] coupled to a zero bias MOM tunnel diode operating at 28.3 THz (10.6 µm). Measured polarization dependence and radiation patterns demonstrate the desirable aspects of this class of antennas at infrared frequencies.

5.2 Antenna Design.

The scaling of operational antennas from microwave to infrared frequencies presents a variety of challenges. The resonant dimensions of the infrared antenna elements and diodes are sub-micron and require resolution beyond the capabilities of traditional photolithography, so that electron-beam lithography is necessary. Also, the unique material properties of dielectrics and metals in this band must be considered. Few low-loss substrate materials exist in the thermal

infrared due to molecular vibrational states. [46] Additionally, metals are known to have significant dispersion and loss in the infrared which reduce antenna performance. [17] These loss mechanisms greatly reduce the propagation length of the infrared radiation in the V-LTSA, reducing the gain of the antenna. Fabrication of the MOM tunnel diode adds additional constraints. We use a shadow evaporation technique [29] which typically sets the minimum dimensions that can be fabricated.

The top view of the antenna-coupled detector is shown in Fig. 26. The endfire V-LTSA is placed with its opening at the cleaved edge of a silicon wafer. The insulating substrate is 1.6 μm of benzo-cyclobutane (BCB), chosen for its low index (n = 1.52) and low loss (k = 0.02) at 28.3 THz. Lead lines are present to measure the dc current generated by the rectifying diode. Optimization of the design was accomplished using commercially available finite element analysis software, Ansoft's High Frequency Structure Simulator (HFSS). The length of the taper is 60 μm, the end taper width is 40 μm, and the feed into the co-planar stripline (CPS) is 0.4 μm wide. The metal trace lines forming the antenna are 0.6 μm wide, while the metal lines forming the CPS are 0.2 μm wide.

The CPS is 20 μm long, with the diode placed inside the CPS 1.5 μm from the taper. The design of the CPS was chosen to simulate a feeding CPS while keeping the dc feed lines far from the diode. The metal sections forming the structure are misaligned by the shadow evaporation technique required to make the MOM tunnel diode. The metal thickness of both the model and the actual device are 30 nm of aluminum, with 6 nm of native aluminum oxide, capped with 30 nm of platinum. The aluminum is deposited with positive angular offset from the substrate's normal; the platinum is deposited with a negative angular offset. This allows a 90 nm x 90 nm

MOM diode to be formed in the center of the CPS, but also causes a 120 nm misalignment of the two metals.

5.3 Antenna Fabrication and Measurement.

The antenna was fabricated on approximately 375 µm thick silicon wafer. 1.6 µm of BCB was spin coated onto the wafer and cured in a nitrogen environment at 250° C. The antenna pattern was written using a Leica EBPG 5000+ Electron Beam Lithographer into a bilayer resist stack of 500nm of MMA capped with 50nm PMMA (Fig.27). The wafer, BCB, and resist are cleaved to provide a straight edge, and the pattern is written across a cleaved edge of the wafer, thus enabling endfire operation.

Figure 27. Not-to-scale front view of the resist and substrate layers shown after lithography and development. The bottom layer is the silicon wafer, covered with a layer of BCB. The green layer (MMA) is more sensitive than the top layer (PMMA), allowing the tunel diode to be created by the shadow evaporation technique.

Once the resist is developed, the wafer is mounted on a custom adjustable stage inside an ultra-high vacuum electron beam evaporator. The tilt stage allows metals to be deposited at positive and negative angles without removing the sample from vacuum. Initially, 30 nm of aluminum are deposited at positive seven degrees. Next, 80 mTorr of pure oxygen are bled into the chamber to allow for controlled oxide layer growth for 30 minutes, resulting in approximately 2 nm of aluminum oxide covering the aluminum surfaces. Then, the stage is tilted *in situ* to an opposing negative angle, and 30 nm of platinum are deposited.

After lifting off the unwanted metals and resist, the device is electrically connected to a five-axis goniometer stage, allowing the device to be centered about the stage's axes of rotation and then rotated in both azimuth and elevation [38]. The test source is a CO_2 laser operating at a wavelength of 10.6 μm (28.3 THz). The signal's polarization is controlled by a wire grid polarizer and a half-wave plate. A pick-off integrated in the optical train of the laser provides a power reference so that the measurement will not be influenced by fluctuations in laser power. A chopper is used to modulate the signal at 1420 Hz to verify the rapid response of the detector and avoid 1/f and 60 Hz noise. The beam from the laser is focused with an F/11 lens to a spot size radius of 115 μm. During alignment, the phase center of the antenna is placed in the center of this spot. The antenna's dc current response is amplified by a low-noise 10X amplifier, and recorded by a lock-in amplifier synchronized to the chopper frequency. This current response is normalized to the reference power, and recorded. The E- and H- plane patterns are generated by varying the azimuth and elevation of the antenna while keeping the laser beam fixed.

TSAs responses are polarization dependent. We varied the polarization of the laser by rotating a half-wave plate, and measured the response of the TSA (Fig. 28). By fitting the data with a $\cos^2(\theta)$ curve, we deduce that the antenna is operating as expected and rule out thermal or photovoltaic effects. The cross-polarized signal is 15% of the co-polarized signal for a 6.7:1 polarization ratio.

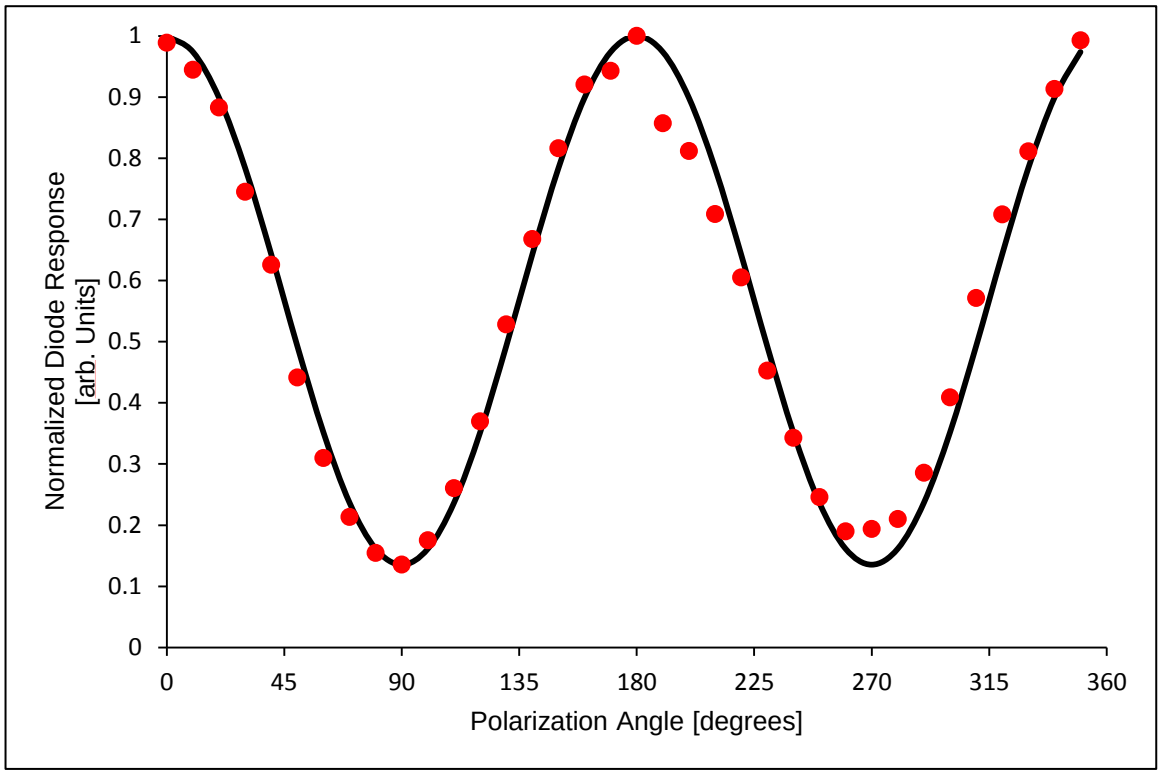

Figure 28. Polarization data points and a cosine-squared curve showing the polarization dependence for this antenna. Data was taken with the device centered at broadside.

To model the radiation pattern of the antenna in receiving mode, a waveport excitation in HFSS accurately predicts the antenna's response at 10.6 μm (28.3 THz), and thus simulates the far-field radiation pattern. From reciprocity, the radiation pattern of the emitting model and the receiving antenna are equivalent. This radiation pattern is used as the expected antenna response.

As shown in Figs. 29(a) and 29(b), the experimental results are in good agreement with the HFSS simulations. The beam patterns show an H-plane -3dB beamwidth of 30°. The E-plane radiation pattern represents the device being held at a constant elevation of -30° (ie, where the H-Plane experiences its maximum). Its -3dB beamwidth is 45°. Previous work in the

millimeter-wave regime achieved near-perfect symmetry and true endfire operation in both planes because materials for the substrate and the superstrate possessed similar indices of refraction, such as air and Styrofoam. [3] The -30° offset of the H-plane patter is caused by a refractive index mismatch between the air superstrate and the BCB/silicon wafer substrate. HFSS predicts that if the superstrate and the substrate are the same material, the infrared antennas will operate in a true endfire-symmetric pattern.

The device's peak response was approximately 8 nA/(W/cm^2). This low responsivity is a result of several loss mechanisms in the substrate and the antenna, impedance mismatches, and the limited nonlinearity of the diode. Future improvements proposed in the diode design and substrate stand to greatly enhance this responsivity.

One promising solution to the responsivity problem is the use of a superstrate, or immersing the antenna into a medium with the same index as the stand-off layer. Not only would the superstrate improve the symmetry of the H-plane about the endfire direction, but HFSS simulations suggest it will raise the responsivity by an order of magnitude. The effects of this superstrate on the diode have not been explicitly studied, but the expected increase in responsivity could make the V-LTSA coupled with a tunnel diode a viable solution for broadband IR-detection.

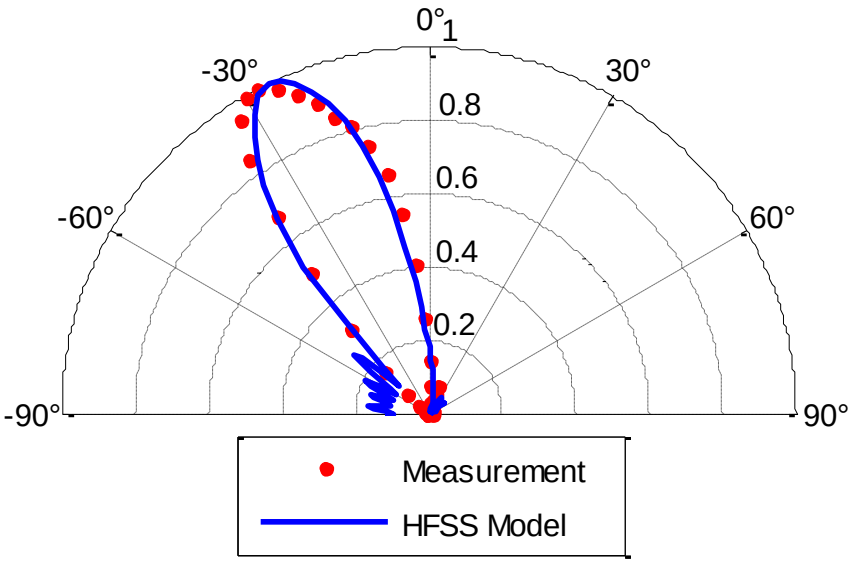

(a)

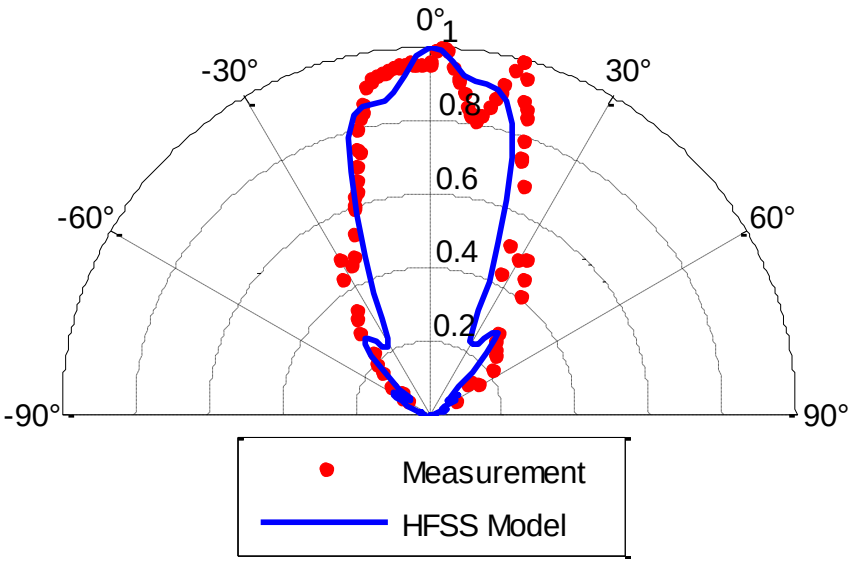

(b)

Figure 29. The modeled (solid line) and measured radiation pattern normalized data points. The H-plane pattern (a) shows a maximum at -30°, while the E-plane pattern (b) is nearly symmetric about the endfire direction.

5.4 Conclusion.

We have constructed an endfire V-LTSA capable of detecting infrared radiation. The antenna has a well-defined beam profile with side-lobes of less than 10% of the maximum signal. The antenna has a beamwidth nearly symmetric in the E- and H-planes.

Further study is needed to understand the effects of the various design parameters to include physical dimensions, choice of substrate, and use of a superstrate for increased responsivity. Also, the advantages and disadvantages of other antenna shapes known to the microwave community (linear TSA, exponential TSA, double exponential TSA, et al.) [8] can now be modeled, fabricated and studied at infrared frequencies. With these advances, we expect that the infrared V-TSA coupled with a tunnel diode will become a desirable sensor for broadband IR detection.

CHAPTER SIX: PHASE RESOLVED NEAR-FIELD IMAGING OF PROPAGATING WAVES IN INFRARED TAPERED SLOT ANTENNAS

6.1. Introduction

Advances in fabrication technology have enabled the development of antennas operating at optical and infrared wavelengths. These devices offer potential improvements for sensing [33, 50-51], energy harvesting [52], diffractive optics [53], and non-linear optics [54]. Many of the designs and analytical techniques developed at radio and microwave frequencies can be scaled down to these shorter wavelengths. Both resonant [55-56] and traveling wave infrared antennas [57] have been demonstrated at infrared frequencies. While planar standing wave antennas such as dipoles [33, 48, 55, 58-59] and Yagi-Uda [60] infrared antennas provide appreciable gain and directional radiation patterns, their bandwidth is fundamentally limited by resonance requirements.

Non-resonant antennas offer the potential for much broader bandwidth. The classical example is the horn antenna which permits an incident plane wave to gradually transform from a freely propagating mode to a confined mode in a waveguide. A tapered slot antenna (TSA) operates similarly but is two dimensional. This makes the TSA compatible with planer layer-by-layer manufacturing techniques, and it has found use at radio frequencies in printed circuit board packages [61]. These manufacturing considerations also make TSAs appealing for use at optical and infrared wavelengths where dimensional considerations require fabrication to be accomplished using thin-film techniques. In addition, the potential for large bandwidth makes TSAs potentially appealing for applications in sensing and energy harvesting.

There are several obstacles that are common to designing infrared antennas. The feature sizes scale with wavelength and are thus much smaller than their RF counterparts. For example, to ensure confinement, the terminating slotline must be substantially smaller than the free-space wavelength, typically on the order of 500 nm for 10.6 μm radiation. Also, the material properties at optical and infrared wavelengths are generally less desirable than at longer wavelengths. At infrared wavelengths, metals exhibit dispersion and ohmic loss [17], and most oxide and polymer substrates have absorptive phonon modes. It is possible to overcome these challenges, but proper design requires deviation from the idealized analytic solutions developed for the microwave spectrum [8]. The lack of well defined analytic solutions requires full-wave numerical simulation, which in turn needs to be experimentally validated.

Interferometric homodyne scattering-type scanning near-field optical microscopy (*s*-SNOM) allows for the direct resolution of the amplitude and phase of the local electric field at nanometer length scales. Recently, this approach has been used to study isolated dipole antennas [48], coplanar striplines excited by dipole antennas [58-59], and Yagi-Uda antennas [60]. It has also been used to study metamaterial surfaces in the infrared [47, 62] as well as propagating surface phonon waves [63].

In this chapter we explore geometries for broadband mode transformation and combination at infrared frequencies through two different TSA designs. The electric field amplitude and phase distributions as measured by *s*-SNOM provide insight into the details of the mode transformation. We show that despite promising results from numerical models, the actual mode transformation is very sensitive to illumination conditions and fine geometric details

governing the phase interaction on different parts of the structure. The accurate characterization of the fields around the TSA facilitates better targeted design of antennas with desired properties.

6.2. TSA Design and Fabrication

The TSA consists of two metal planes, either free standing or supported by a substrate, with a tapered slotline between the planes. These metal planes act as the outer edge of a waveguide, gradually confining coupled radiation into the slotline. Conventionally, the antenna is intended to operate in an endfire fashion, with radiation entering the aperture along the same axis as the slotline. In the infrared version of the TSA, the metal planes are not mechanically strong enough to be free standing and must be supported by a substrate. In this work the TSA is separated from a silicon substrate by a layer of benzocyclobutene (BCB). The BCB is added because it has a lower index than Si (n_{BCB}=1.57 at 10.6 μm) and is an electrical insulator. The latter point is essential when a sensing element, such as a metal-oxide-metal (MOM) diode, is added to the slotline [33].

Unfortunately the use of a MOM diode prevents overcoating the TSA with a matching dielectric. Because the metal planes are not bounded by a uniform dielectric (as they would be in a conventional RF TSA) the behavior of the antenna is significantly modified. We previously showed that IR TSAs bounded with a BCB substrate and air superstrate have a maximum responsivitiy 30° above the endfire direction (60° from the surface normal) [57]. Because this behavior is a significant departure from established RF designs we choose to study it with *s*-SNOM.

Two different TSAs were designed and fabricated for this study and are shown in Fig. 1. The first device is a traditional linear tapered slot antenna (LTSA) (Fig. 30a) with a tapered slot cut from a rectangular metal plane. This antenna has been shown to work in the microwave region, and is expected to sustain surface waves on the metal and parallel plate modes on the sides [8]. The second is a V-shaped linear tapered slot antenna (V-LTSA) (Fig. 30b) similar to earlier designs built and characterized in [57]. The devices are built on 1.5 μm of BCB which is spin coated onto a [001] crystalline silicon wafer. The dimensions of the tapered slot are identical for both devices. The opening aperture is 12.5 μm across, and the length of the taper is 30 μm. The slotline is 10 μm long and 500 nm wide. The V-shaped antenna has 200 nm wide wires in the slotline, and 600 nm wide wires in the antenna arms in order to maintain the design of previously reported devices. The LTSA slotline is cut from a metal plane that is 29.5 μm wide. These patterns are written into an MMA/PMMA stack using an electron-beam lithography system. After depositing a 5 nm titanium adhesion layer, 60 nm of gold are deposited using a high-vacuum electron-beam evaporator. Residual resist is lifted off, leaving the gold antenna patterns on BCB.

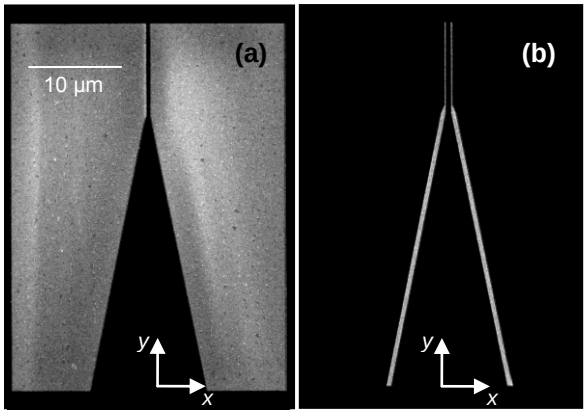

Figure 30. SEM images of (a) the Linear Tapered Slot Antenna (LTSA) and (b) the V-shaped Linear Tapered Slot Antenna (V-LTSA).

It should be noted that these antennas differ from the design previously studied [57], since there is no detector or feedpoint in the slotline, and the BCB substrate extends in the endfire direction. Historically, the taper termination coincides with the edge of the substrate. Their length is shorter than previously reported devices in order to ensure that the device dimensions are on the same scale as the exciting radiation spot size (60 μm). Despite these discrepancies, wave propagation patterns and antenna response similar to the tested devices are expected.

6.3. Operation of the *s*-SNOM system

A schematic of the *s*-SNOM system is shown in Fig. 31. Our instrument design is similar to the *s*-SNOM used in [47-48, 58]. The *s*-SNOM system uses an atomic force microscope (Bruker, INNOVA) operating in tapping mode. In this study we use an Arrow NCPt (Nanoworld) silicon AFM probe which is platinum coated in order to enhance the scattering of the near-field. The cantilever dithers at ~270 kHz with an amplitude of ~20 nm as the antenna is raster scanned beneath the tip. A closed-loop control maintains a constant force interaction between the sample and tip during scanning. The tip is illuminated with an s-polarized (with respect to the sample) 10.6 μm CO_2 laser focused to an elliptical spot with a minor axis of 60 μm. The illumination strikes the sample with a $\theta = 60°$ angle of incidence relative to the surface normal which coincides with the maximum response direction for the TSA.

During scanning the TSA is excited by the incident laser beam. Energy couples to propagating waves along the antenna. This results in electric fields closely bound to the surface of the antenna. The probe interacts with these fields and scatters some of the energy back into propagating light. A portion of the tip-scattered light is collected by the same objective used to

focus the incident laser beam and passes through a beam splitter. A wire-grid polarizer ensures that only the p-polarized light caused by scattering is collected and mixed with a reference signal. This cross-polarization selectivity reduces the signal caused by scattering events other than the tip. The resulting interference is recorded using a liquid nitrogen-cooled HgCdTe detector which is coupled to a lock-in amplifier operating at the second harmonic of the dithering frequency. Previous studies have shown that this configuration results in a signal that is closely correlated to the z-component (normal to the surface) of the electric field [48, 58-61]. The signal is effectively proportional to

$$I \propto \left|E_{nf} + E_{ref}\right|^2 = \left|E_{nf}\right|^2 + \left|E_{ref}\right|^2 + 2\left|E_{nf} \cdot E_{ref}\right| \cos\varphi \tag{48}$$

where $\varphi = \varphi_{nf} - d \cdot 4\pi/\lambda_0$, denoting the difference between the reference phase and the phase of the near-field electric field at the point in the sample directly beneath the probe. By adjusting the delay length d of the reference beam we can control the phase at which the electric field is sampled. We compile multiple images at different phases and perform a least-squares fit on a point-by-point basis to extract phase. This procedure results in recording only the portion of the field that varies with respect to the phase of the reference beam and thus accomplishes some of the background suppression that would be provided by dithering the reference mirror [63].

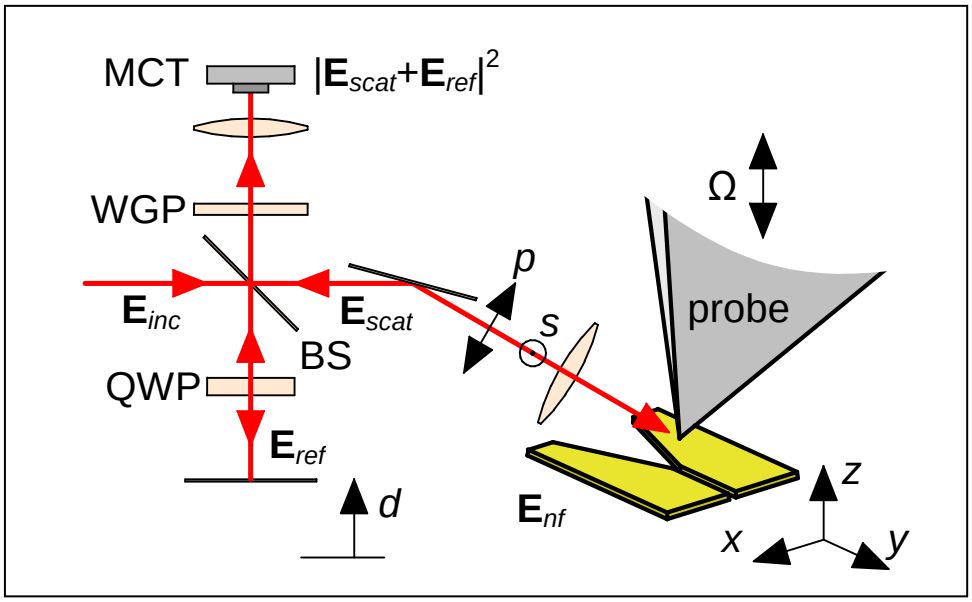

Figure 31. Schematic of scattering-type Scanning Near-field Optical Microscope (*s*-SNOM).

Because the antenna extends several wavelengths and the sample must be translated over the entire length to image it, we observe a phase shift during scanning [64]. Initially, the antenna is excited at its entrance aperture (the *x*-axis in Fig. 30). As the antenna is scanned in the *y*-direction the phase of the incident light at the aperture shifts due to the off-normal excitation. This can be accounted for in post-processing so that

$$\varphi = \varphi_0 - y \cdot k_{0,y} \tag{49a}$$

where

$$k_{0,y} = k_0 \sin\theta \,. \tag{49b}$$

6.4. Results

Figure 32 shows experimental results for the linear TSA (SEM image in Fig. 30a). We scanned the antenna seven times at increments of $\Delta\varphi = 45°$ ($\Delta d = 1.325$ μm). During the course

of scanning, the *s*-SNOM simultaneously records AFM data, which is shown for one of the scans in Fig. 32a. Each image shows a 45×45 μm^2 scan field. Fig.s 32 b-d show data extracted from a least-squares fit of the raw *s*-SNOM data which removes some artifacts of self-homodyne interference. The amplitude plot (Fig. 32b) is normalized to the maximum signal over the scan. Fig. 32c shows the phase data as recorded by the *s*-SNOM. When this is corrected with Eq. 49 we obtain the image in Fig. 32d at a single phase. If this is animated over phase we clearly see waves propagating over the surface of the antenna in the $+y$ direction.

We modeled the antenna using a full-wave finite element method solver (HFSS, ANSYS Inc.). To increase simulation accuracy we included material properties acquired for the materials at 10.6 μm using spectral ellipsometery. We modeled the excitation as a Gaussian beam focused on the center of the entrance aperture (the origin in Figs 30a and 30a). The amplitude of the z-component of the electric field 5 nm above the top surface of the antenna is plotted in Fig. 32e. This is normalized to the electric field of the incident field. Fig. 32f shows the phase map obtained from simulation after adding the scanning induced phase delay. Finally, Fig. 32g shows the field at a given phase angle without the simulation the scanning phase so that it corresponds directly to Fig. 32d.

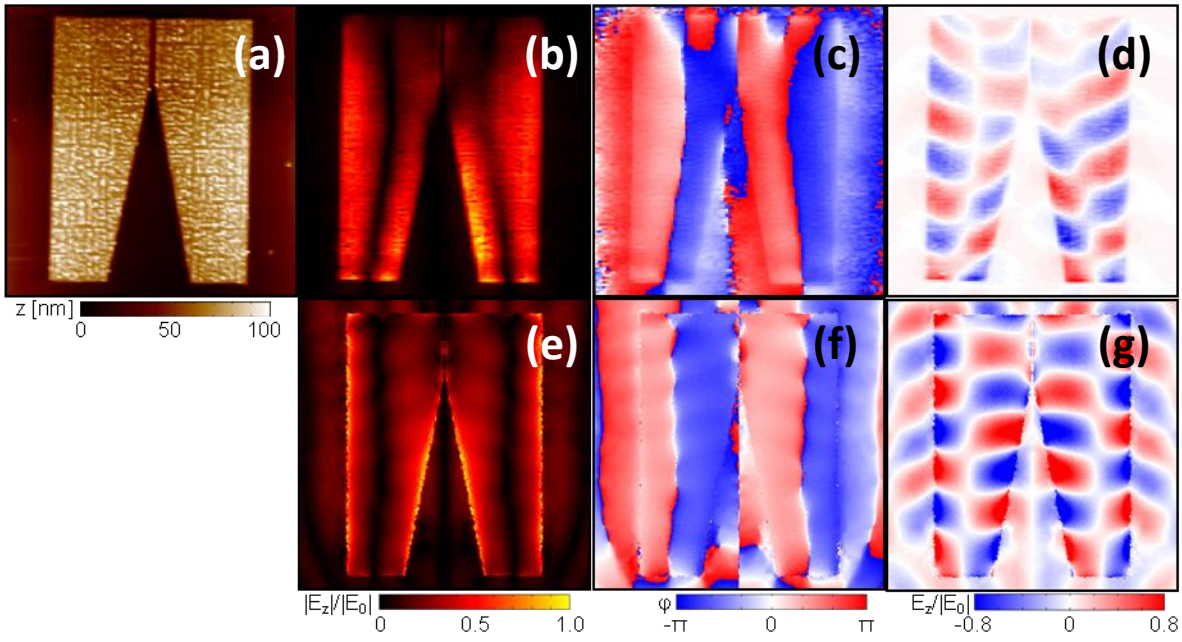

Figure 32. Experimental *s*-SNOM results for LTSA compared to simulation (a) AFM acquired topography (b) near-field amplitude (c) near-field phase (d) local field at φ=0° corrected for scanning, (e) simulated $|E_z|$ 5 nm above antenna (f) phase of $|E_z|$ corrected for scanning and (g) $|E_z|$ at φ=0°.

We repeated both the *s*-SNOM experiment and the simulation for the V-LTSA. Simulation predicts that the response from this antenna (how much light is coupled into the slot portion of the waveguide) will be greater than the LTSA. In the V-LTSA, the single-wire waveguide modes are combined and transformed into coplanar strip transmission line modes as the antenna narrows [58-59]. The results for the V-LTSA are shown in Fig. 33. Because the features are finer for this antenna, a second set of images was taken closer to the entry point of the waveguide portion of the antenna. Fig.s 33 a-d and Figs. 33 e-k show 45×45 μm^2 and 25×25 μm^2 field-scans, respectively. The HFSS simulation is setup identically to Fig. 32 e-g, with the incident laser beam centered on the origin. The simulation of the V-LTSA predicts that there is minimal field away from the antenna structure. This agrees with the experiment. The minimal

field away from the metal makes the resolution of the phase prone to error in this region. However, there is good phase agreement between the experiment and the simulation in regions above the antenna.

Figs. 32 and 33 show good qualitative agreement between simulation and experiment in both phase and amplitude. There are the same number of wave cycles along the inner edges of the TSA in each figure, and the linear null region that runs the length of both antennas is correctly predicted by simulation. The measured field magnitude in the slotline is less than predicted by simulation; we attribute this to attenuation of the field in the antenna. The phase interaction of the light on opposite sides of the waveguide may play a part in the increased attenuation. While the waveguide mode for the LTSA in the simulation (Fig. 32g) is asymmetric with respect to phase across the waveguide, the measurement (Fig. 32d) exhibits a substantial longitudinal field component, indicating that attainment of the proper phase for mode transformation at the constriction is very sensitive to illumination conditions and fine details of the geometry of the structure.

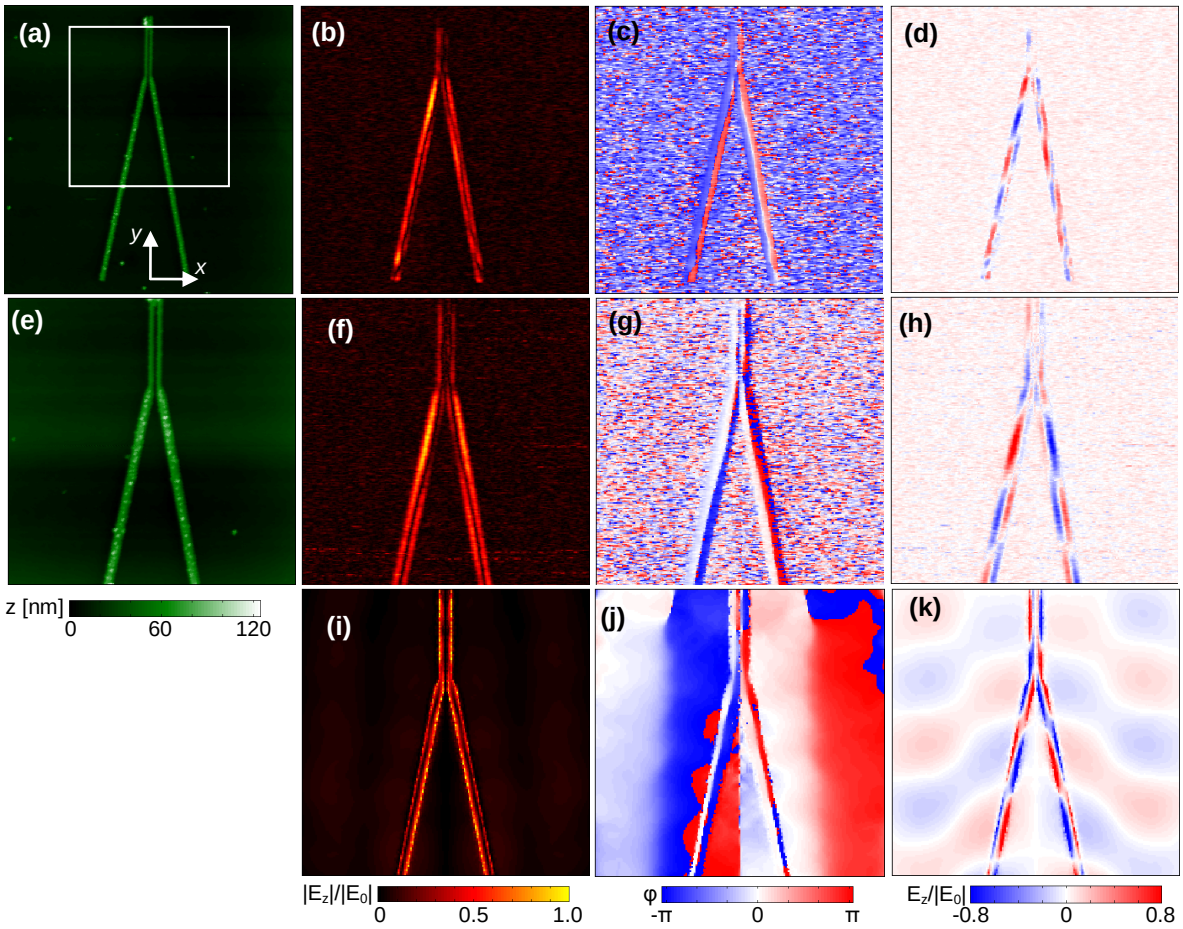

Figure 33. Experimental *s*-SNOM results for V-LTSA compared to simulation (a,e) AFM acquired topography (b,f) near-field amplitude (c,g) near-field phase (d,h) local field at φ=0° corrected for scanning, (i) simulated $|E_z|$ 5 nm above antenna (j) phase of $|E_z|$ corrected for scanning and (k) $|E_z|$ at φ=0°. Figs. (e-k) show a closer image of the area in (a).

The measured near-field V-LTSA (Fig. 33h) agrees roughly with the numerical simulation (Fig. 33k). On the open end of the structure, the light is guided as two single-wire modes opposite in phase. At the constriction, the modes converge, forming a single dual-wire mode similar to that of a coplanar stripline. In this way, the V-LTSA can be considered a mode combiner. However, the combined mode in the slotline is attenuated more than expected, possibly due to the effects of sharp features at the corner near the convergence point.

In both experiment and simulation the V-LTSA shows more pronounced fields in the terminated slotline portion of the antennas. However, this is not noticeably higher than the field at the entrance aperture suggesting that these antennas do not have a high gain. Moreover, the difference in refractive index between the BCB substrate and the air superstrate cause the antenna to act as an inefficient leaky waveguide.[8] The losses inherent to the structure prevent any noticeable increase in field magnitude as the signal progresses along the tapered region of the antenna, both in simulation and in actual measurement. Simulations of the structure with matching dielectric above the TSA (not shown) predict much better response as well as a peak of directivity in the endfire direction. However, it would not be possible to study these antennas directly with *s*-SNOM because the fields would be confined within the dielectric.

We note that the *s*-SNOM technique provides fine structure measurement of spatially transient fields, allowing high spatial resolution in the resulting images. This high spatial resolution allows us to visualize the mode transformation occurring along the taper into the slotline. Additionally, the high resolution of the image allows point by point comparison to simulation, allowing validation of design parameters. The simulation results are for a beam centered on the entrance aperture. The fact that the experiment agrees with this result indicates that the coupling occurs at this entrance aperture for the physical antenna. That is, we would expect discrepancies if the coupling was distributed over the length of the antenna. The simulation predicts greater fields in the area surrounding the antenna than are observed experimentally. This indicates that probe is more efficient scattering the field when it is directly above the metal antenna. This agrees with analytic models [65] of the *s*-SNOM process that model the antenna as an image plane for the probe.

6.5. Conclusion

We have shown that the near fields of a non-resonant tapered slot antennas of multi-wavelength dimensions can be accurately imaged using a scattering *s*-SNOM system. The resulting images show high spatial resolution, allowing for accurate magnitude and phase imaging for fine features. These results are in good agreement with numerical simulation. This serves to validate numerical models of the structure as well as the correspondence of the normal component of near-surface electric field to the *s*-SNOM signal, but it highlights the differences between ideal structures and actual ones, where the device behavior can be very sensitive to illumination conditions and fine geometrical details. Future work to improve infrared TSAs should focus on improving coupling efficiency. This will increase the magnitude of the near-fields in the terminating slotline, allowing for improved sensing. In order to increase the coupling efficiency, the antenna needs to be placed between a substrate and a superstrate that have similar indices of refraction. One method of doing this is reducing the index of the substrate by using a substance such as aerogel. The other method is using a higher index superstrate to coat the antenna.

CHAPTER SEVEN: EFFECTS OF TAPER LENGTH, FLARE ANGLE AND SUBSTRATE CONFIGURATION ON THE RADIATION PATTERNS OF INFRARED TAPERED SLOT ANTENNAS

7.1 Introduction

The tapered slot antenna (TSA) was developed in 1979 at microwave frequencies as a feed element for a slotline waveguide [1,2]. It is notable for its low profile, broadband response and rotationally symmetric beam shape. In general, a TSA consists of a slotline formed by two coplanar conducting sheets with the slotline's width increasing as it approaches the endfire edge of the conducting sheets [1]. Common variations of the TSA include the Vivaldi Aerial, the linear tapered slot antenna (LTSA) and the constant-width tapered slot antenna (CTSA) [3]. Numerous parametric studies to determine the effects of the antenna's length and aperture width, as well as the substrate configuration, have been conducted at microwave frequencies. In addition, mathematical models describing the antenna's operation have also been derived [12-14,16].

Our goal is to extend TSA operation to mid-infrared frequencies where its broadband response makes it appealing for sensing and energy harvesting applications. This requires overcoming significant obstacles, notably the sub-micron critical dimensions of the antennas and detectors, the lower conductivity and higher dispersion of metals in the infrared [17], and the lack of low index, low-loss substrates over this spectral range. Previously, we demonstrated the use of nanofabrication techniques to create an infrared TSA coupled with a metal-oxide-metal (MOM) rectifying diode to produce a well-defined radiation pattern [57].

Analytic models developed for TSAs at microwave frequencies [12-14, 16, 19] fail to accurately predict the performance in the infrared. These models assume the metallic elements to

be perfect conductors, a poor representation of their behavior in the infrared [5, 18, 22]. In addition, previous models relied on broadband, thin substrates with very low refractive index (1.0 to 1.2) and negligible loss which are not readily available at infrared frequencies. Despite these deficiencies, microwave models do provide guidance for designing TSAs. For example, to achieve a symmetric radiation pattern the taper length should be between two and ten wavelengths and the opening aperture should be at least half a wavelength wide.

TSAs can be designed to operate in either an end-fire mode or as a leaky-wave antenna depending on the effective index of the substrate. In an endfire antenna, incident radiation at the entrance aperture excites a propagating TE mode which is gradually confined to the slot line. This has been shown to produce more than a 100:1 polarization ratio [22] and generates a symmetric radiation pattern about the endfire direction. However, when there is a substantial mismatch between the indices of media above and below the TSA, the structure acts a leaky-wave antenna, with input/output coupling distributed over the length of the taper. This shifts the radiation pattern toward the lower-index medium [8]. All previous infrared TSAs have operated in the leaky-wave mode [57, 66] with a measured H-plane radiation pattern having a maximum shifted by 30° from the end-fire direction.

In this paper we perform parametric studies to determine the effect of TSA geometry on far-field radiation patterns. Because the TSA is a non-resonant structure, the radiation pattern is relatively insensitive to changes in the taper geometry. However, a significant improvement in performance is achieved by reducing the index mismatch between the substrate and the superstrate by adding a dielectric over the antenna, resulting in a four times increase in antenna gain.

7.2 Device Fabrication, Modeling and Testing.

Each antenna, integrated with a MOM diode, is formed using a shadow evaporation method in a single lithographic process. Details on the fabrication process can be seen in [31]. Fig. 1 shows an example of a fabricated antenna. It consists of 600 nm wide taper lines, feeding a 400 nm wide coplanar stripline, forming a V-shaped linear TSA (V-LTSA). The wires forming the stripline are 200 nm wide. The diode is placed in the coplanar stripline 1.5 μm from the end of the taper. The stripline is 20 μm long, and terminates at electrical feedlines which are used to electrically connect the device. In this paper we focus on identifying the effects of varying the taper length, L, and the taper angle, α, as shown in Fig. 34.

The antenna is fabricated on top of a silicon wafer. Silicon wafers are chosen as substrates because they are inexpensive, non-hazardous, and non-reactive with most resists and solvents. In addition, they cleave precisely across crystalline planes. However, the use of a semiconducting substrate requires an insulating thin film to prevent shorting of the MOM diodes. For 10.6 μm radiation, benzocyclobutene (BCB) is used because it has a low refractive index (n = 1.57) and a low loss (k = 0.02) at 10.6 μm. In addition, it is easy to deposit and has good adhesion to the silicon substrate. For the TSAs presented in this paper, a 1.6 μm film of BCB is spin coated and cured onto a 3" [001] silicon wafer. A bilayer resist stack (450 nm MMA-E9 capped with 50 nm PMMA A2) is spun on top of the BCB. The wafer is cleaved along the crystalline axis, and the cleaved wafer is aligned so that the pattern is written with the antenna arms extending across the cleaved edge. By accurately controlling the location of the pattern's center with respect to the cleaved edge, different taper lengths are produced.

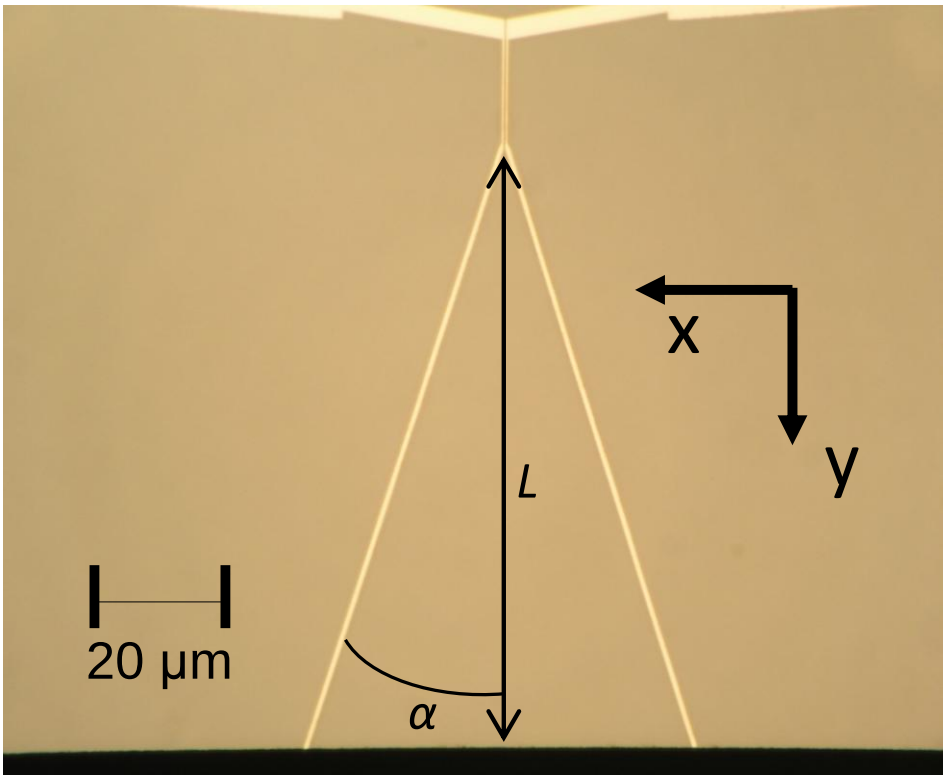

Figure 34. The V-LTSA with taper length *L*=100 µm and taper angle α=18.5°.

The device is patterned using Vistec EBPG 5000+ electron beam lithographer operating with an accelerating voltage of 50 kV. An 80 nm gap centered in the slotline portion of the pattern causes a PMMA bridge to be formed because the underlying MMA becomes developed by scattered electrons. This bridge is critical for the shadow evaporation technique of forming MOM diodes. After developing, 30 nm of aluminum is deposited using an electron beam evaporator with the device tilted at +7° so that the aluminum is deposited beneath the PMMA bridge. The aluminum is oxidized in situ at 80 mTorr for 30 minutes to allow an oxide layer to form. Previous work has shown the thickness of this oxide layer is 2-6 nm. The device is then tilted to -7° and 30 nm of platinum is deposited. After lifting off the residual resist, the device is

mechanically and electrically attached to a chip carrier so that the endfire direction is parallel to the surface normal of the carrier.

The intrinsic field in the diode, proportional to the work-function difference between the two metals [30], permits its operation at zero bias. The oxide serves as a potential barrier to the movement of electrons. The intrinsic electric field created by the work-function difference is insufficient to excite an appreciable number of electrons across the potential barrier of the oxide layer. However, when an oscillating electric field is applied, electrons are preferentially moved in the direction of the intrinsic electric field. Thus, the diode acts as a half-wave rectification element for electromagnetic waves [30]. Aluminum and platinum were selected because of the large difference in their work functions and because native aluminum oxide growth can be controlled in-situ. Because we are using only one lithographic process, these two metals will also form the antenna element.

MOM diodes must have a small cross-sectional area (90 nm x 90 nm) to ensure the diode's cutoff frequency exceeds the frequency of operation [30]. This makes the diodes sensitive to imperfections in the materials such as grain size and precise location of the metals involved. These imperfections cause non-uniformities in the thickness of the oxide and the size of the metal overlap area, which, in-turn, result in a large range of responsivities. This makes a precise device-to-device comparison of responsivity difficult [32]. However, normalized radiation patterns can be used to evaluate the effectiveness of a given TSA design.

The devices are modeled using HFSS (ANSYS), a finite element solver with an adaptive mesh. Material properties used for the substrate, insulating thin film, and metals were characterized using a spectrographic ellipsometer (J.A. Woollam IR VASE). A waveport source

excites the stripline at the location of the MOM diode. Finite element analysis yields electric and magnetic fields throughout the problem region, from which radiation (far-field) quantities are computed. Far-field radiation patterns are predicted by computing radiated power as a function of angle which, by reciprocity, also describes the expected angular receiving properties of the antenna. Special attention must be paid to the boundaries of the model. Because the silicon wafer is not absorptive at 10.6 μm, the field within the thick substrate must be accounted for. If the wafer is not sufficiently thick in the model, the H-plane pattern will experience diffractive effects arising from sharp edges in the substrate model. Similarly, the modeled antenna response is dependent on how far the substrate element extends laterally past the edges of the arms. If the edges are too close, the E-plane pattern will be distorted by diffractive effects. In both cases, we find that two wavelengths of material coupled with absorbing boundary conditions are sufficient to allow accurate modeling of radiation patterns. The far-field response of the antenna is simulated and compared to experimental radiation patterns to ensure the model's validity.

The chip carrier with the device is mounted to a goniometer with eight degrees of freedom, and then electrically connected to a lock-in amplifier. A CO_2 beam is sent through a fixed wire grid polarizer to define the polarization of the signal. A pick-off sends some radiation to a power meter so that the signal can be normalized to the input power. The beam continues through a half wave plate which allows us to vary the polarization of the signal, then through a chopper operating at 1340 Hz which triggers the lock-in amplifier. The beam is finally focused onto the device with a spot size of 230 μm. The phase center of the antenna is centered at the axis of rotation of the goniometer [38] in order to prevent changes in signal caused by translation of the phase center.

7.3 Results and Discussion

Radiation power patterns are generated by measuring the diode's current output at various angles of rotation [67]. Fig. 35 shows the simulated and experimental far-field radiation pattern for the device in Fig. 34. Note that the azimuth and elevation angles, θ and φ, are measured from the endfire direction. The polar plots contain two normalized radiation patterns. The HFSS model (blue line) is derived by calculating the square of the far-field electric field caused by the waveport at various angles. The measurements (red dots) are measured current values produced by the diode at various angles of incidence caused by rotating the goniometer.

The purpose of the parameter study was to determine the effect of geometry on the normalized radiation pattern in both the E-plane and the H-plane. By varying the length of the taper or the angle of the taper, we expect to see corresponding changes to the radiation patterns which will allow us to tailor future infrared V-LTSAs to desired radiation patterns.

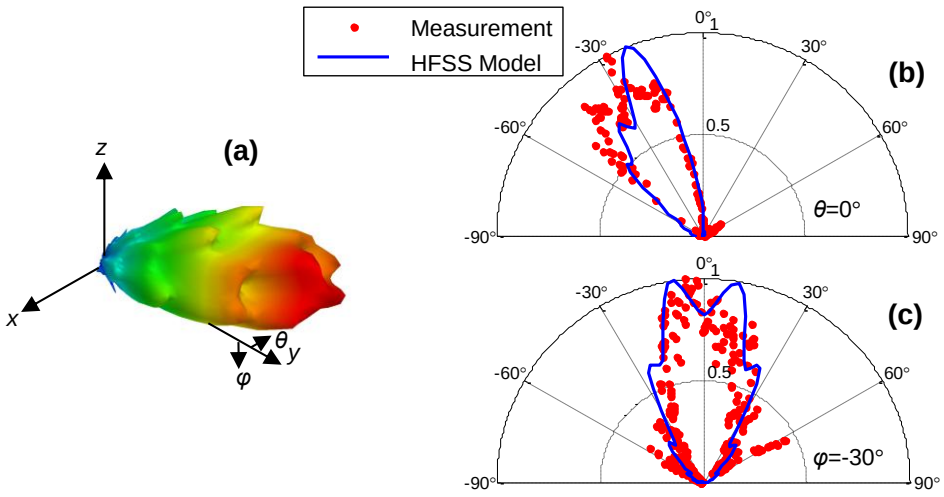

Figure 35. Radiation patterns for antenna with a taper length (L) of 100 µm and a taper angle (α) of 18.5°. (a) Three dimensional view from HFSS model. (b) normalized H-plane pattern. (c) normalized E-plane pattern at an elevation angle of φ = -30°.

Fig. 36 shows the HFSS model results and measured values for the full width at half maximum (FWHM) beam width for both the H-plane and the E-plane (taken at a constant azimuth angle of -30°). The taper angle of these antennas remained fixed at 18.5°. Antennas with taper lengths longer than 125 μm (8.5 wavelengths in the thin film) failed to create a single identifiable central beam and are not shown. As the taper length increases, the H-plane narrows as the taper length approaches two wavelengths, and becomes fairly constant beyond two wavelengths. The E-plane pattern shows the beam width varying rapidly as the taper length increases. In the regions of greatest angular width, the central lobe becomes reduced and shoulders become greater due to destructive interference from the increased range of phases over the wider aperture. This results in a wide radiation pattern with two shoulders as peaks and a lower central maximum. This process is repeated as the taper length increases which suggests that lengths less than four wavelengths must be used to ensure that a single main lobe is achieved in the E-plane radiation pattern. Taper length values in this range also provide the best symmetry between E-plane and H-plane radiation pattern sizes.

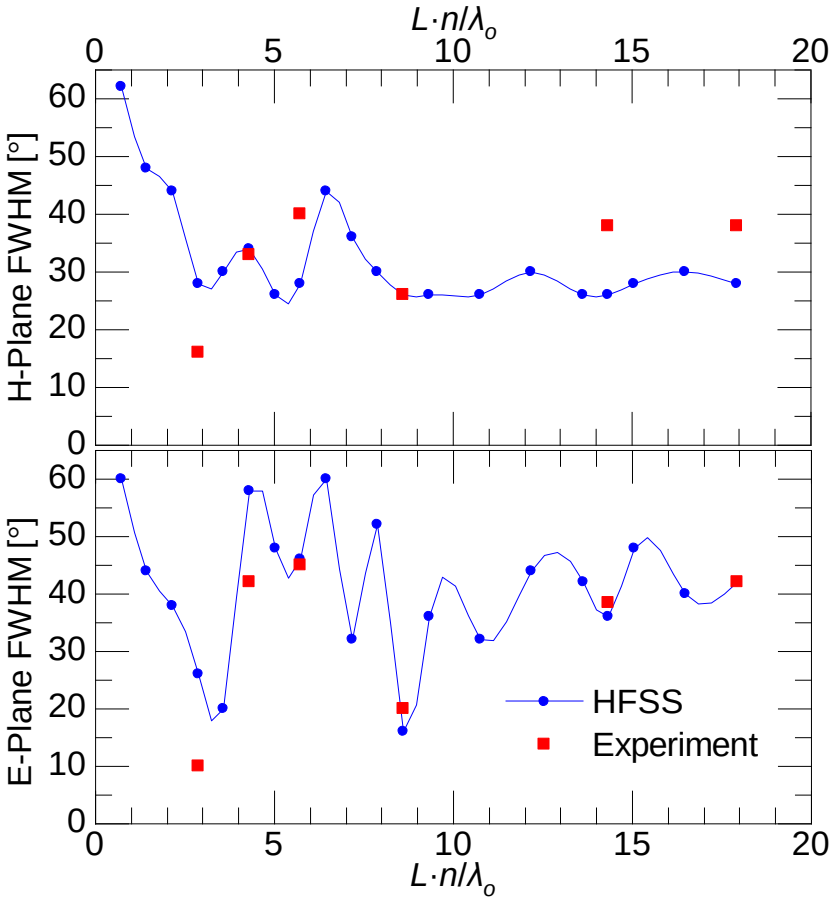

Figure 36. Central lobe beam width (FWHM) of H-plane and E-plane patterns as a function of taper length.

Fig. 37 shows the simulated maximum far-field response as a function of length. The data are the maximum field magnitudes in the H-plane for various taper lengths in the HFSS model. The maximum around three wavelengths is to be expected, as this is also near the minimum angular width for the H-plane and the E-plane from Fig. 36. However, the predicted response becomes nearly constant at longer taper lengths. This can be explained by an examination of power entering the system versus losses inherent in the system. As the taper length increases, the aperture increases linearly, allowing more radiation to enter the antenna, but the propagation

losses increase linearly with the length. The two processes offset themselves. Thus, increasing the taper length has the effects of creating beams with degraded beam shapes and does not increase the responsivity of the devices. The optimal length for beam symmetry and responsivity is predicted to be about 3 wavelengths (25 μm for the given structure.)

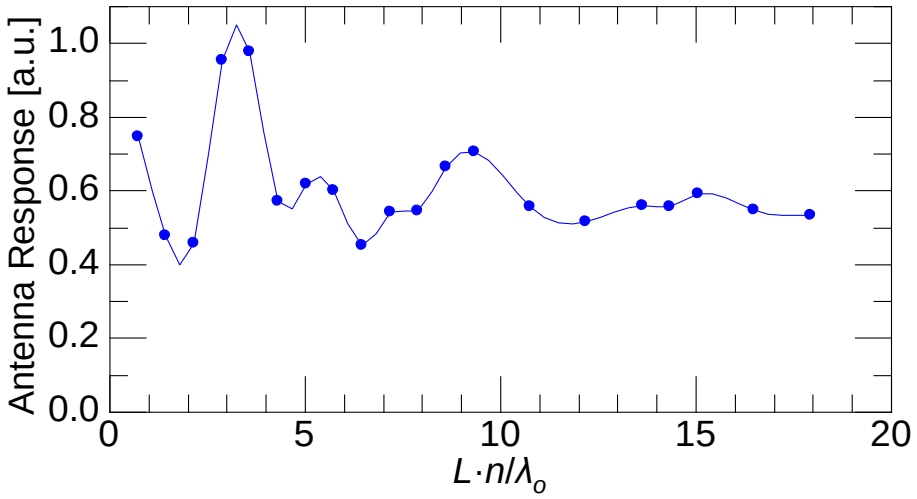

Figure 37. Expected maximum antenna response for various taper lengths.

Next, the taper length (L) was fixed at 60 μm to match previously published designs [57], while the taper half-angle (α) was increased from 5 to 60 degrees. The resulting FWHM beam widths are shown in Fig. 38. As was the case for the taper length, increasing the taper angle had minimal effect on the H-plane beam width, but caused the E-plane pattern to expand. However, modeling results seen in Fig. 39 show that the expected antenna responsivity does not change much. This is because there is a higher rate of impedance change at larger taper angles, resulting in more reflected power. This increased loss is balanced by a larger aperture, with the net result being little change in responsivity with angle. From this data, we can define an optimal taper

half-angle of about 20° for a 60 µm taper length. This results in the narrowest E-plane pattern, making symmetry with the H-plane pattern possible. Larger angles will only increase the width of the E-plane pattern without an increase in response, and smaller angles will decrease the response.

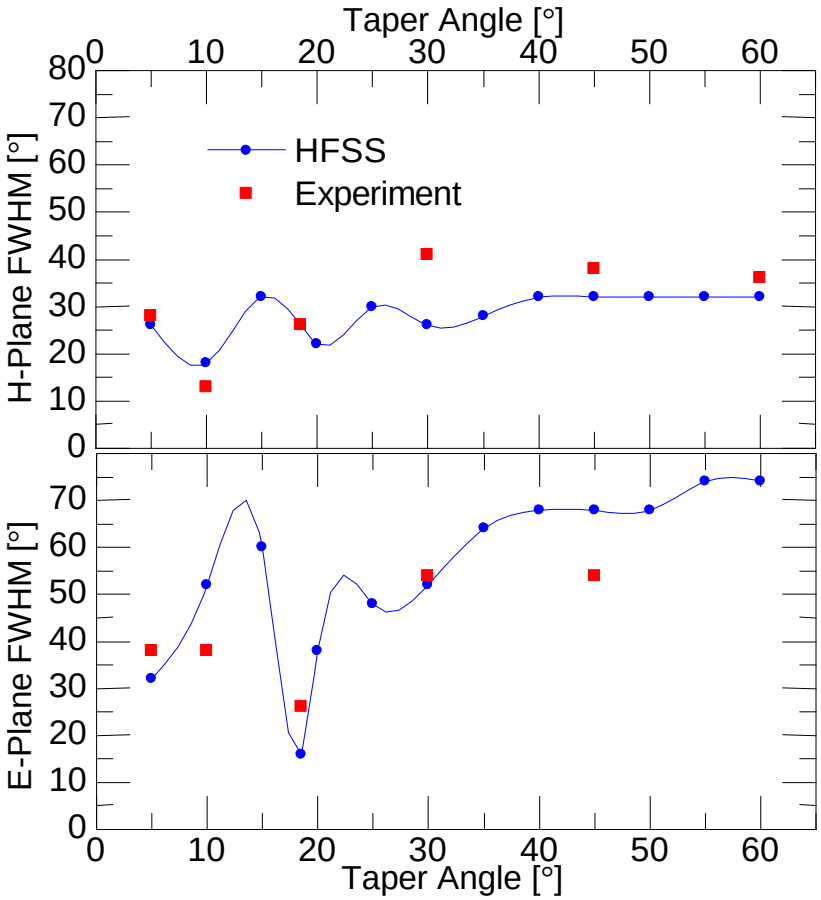

Figure 38. Central lobe beam width (FWHM) of H-plane and E-plane patterns as a function of taper angle.

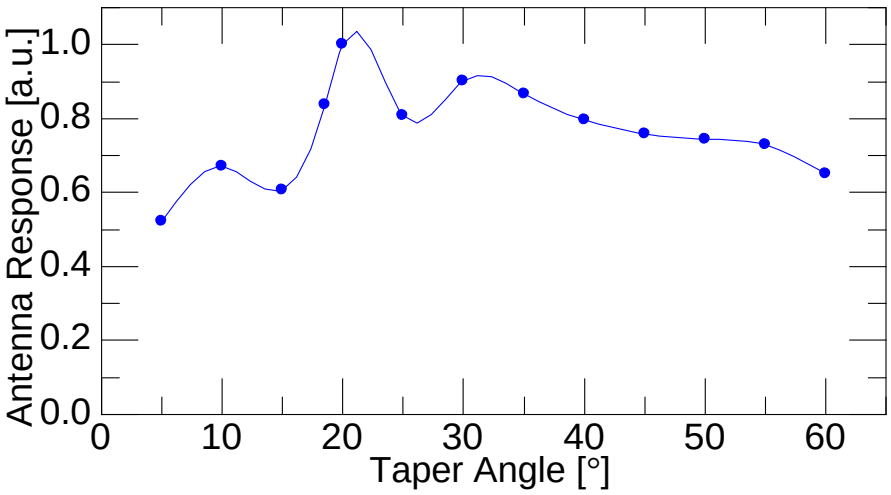

Figure 39. Expected maximum antenna response for various taper angles.

The data presented to this point have been representative of various infrared V-LTSAs set on top of a BCB thin film on a Si substrate. We expect that these antennas will operate as leaky antennas because of low confinement in the thin film and substrate that make up the tapered slot. The index mismatch with the air superstrate is too great to maintain tightly-bound modes between the metal antenna elements, so energy will couple to radiating modes along the structure causing the maximum response to be at approximately $\varphi = -30°$.

In an attempt to minimize this index difference, we deposited a BCB superstrate over the antenna. The diodes proved too fragile to survive spinning and curing BCB. Instead, the antenna structure was dipped into the BCB and allowed to air dry at room temperature for several days. The resulting radiation pattern is shown in Fig. 40, and is compared to an uncoated antenna. The radiation pattern of the coated antenna has significantly higher gain that that for the uncoated antenna and the beam retains the same maximum response direction in the H-plane. In both planes, the response of the antenna increased by a factor of four. This suggests that the increased

response in the coated antenna is caused by greater confinement of the propagating wave. For the coated antenna the index mismatch occurs at the BCB – silicon interface and not at the antenna. Reducing the rate of re-radiation from the antenna permits more energy to reach the diode and excite a response.

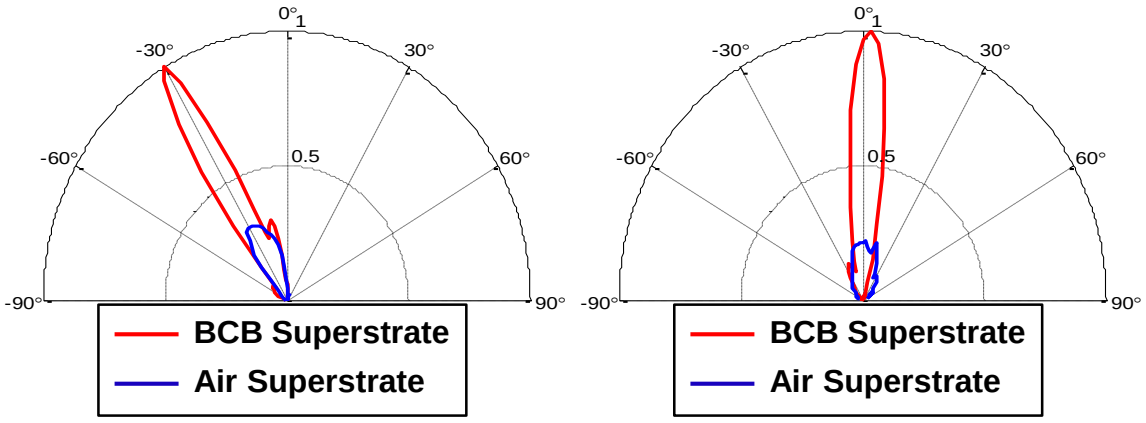

(a) (b)

Figure 40. (a) H-plane and (b) E-plane normalized radiation patterns for antenna with BCB superstrate with air substrate patterns shown for comparison.

7.4 Conclusions

We have shown that the geometrical design of the taper influences the radiation pattern of the infrared V-LTSA. There is a direct correlation between the size of the endfire aperture and the width of the E-plane radiation pattern. A taper length of 2-6 free space wavelengths provides the best definition of the central lobe of the radiation pattern, with a taper length of about 3 wavelengths providing the narrowest radiation patterns. Taper angles between 10 and 30 degrees allow the designer to increase the collecting aperture size without degrading beam quality.

We also developed a method of applying a superstrate to the antenna that significantly increases the antenna's response, resulting in higher-gain radiation patterns. Future work should focus on increasing responsivity and creating a true endfire antenna. Both of these goals can be accomplished by decreasing the effective index difference between the substrate and the superstrate while continuing to minimize loss. While the most straightforward solution to this index mismatch is the development of very low index substrates, this is a difficult task in the infrared. Several variations have been suggested [9-11, 20-21] to decrease the effective index of the substrate, such as placing plasmonic bandgaps or perfect magnetic conductors between the insulating thin film and the substrate.

CHAPTER EIGHT: FUTURE WORK

The work in this dissertation has resulted in successfully modeled, fabricated and tested infrared V-LTSAs operating as leaky antennas. While these accomplishments have been satisfying, additional challenges lie ahead for the further understanding and improvement of these antenna elements. I have identified four especially vexing subjects in hopes that future efforts in analysis and fabrication can further the application of these devices.

8.1 Polarization Analysis

Polarization rejection is one figure of merit used in the determination of how well-behaved a fabricated TSA will respond. The lack of polarization rejection is proof that a portion of signal is being generated by thermal effects, which have not been included in the creation of the model. Additionally, we know that TSAs in the microwave regime are essentially TE mode transformers, rejecting the TM modes. If this were true for the leaky wave TSA antenna, we would expect to see maxima every 180°, and minimum 90° from each maxima. We would also expect the maxima to occur at the TE orientation of the antenna.

What is observed is quite different from this ideal. While all of the TSAs that I measured showed some degree of polarization rejection, the maxima very rarely parallel to the TE orientation. Some showed maxima at every ninety degrees. An especially difficult to understand data set (for a 300 μm taper length) produced different radiation patterns for orthogonal polarizations (Fig. 41).

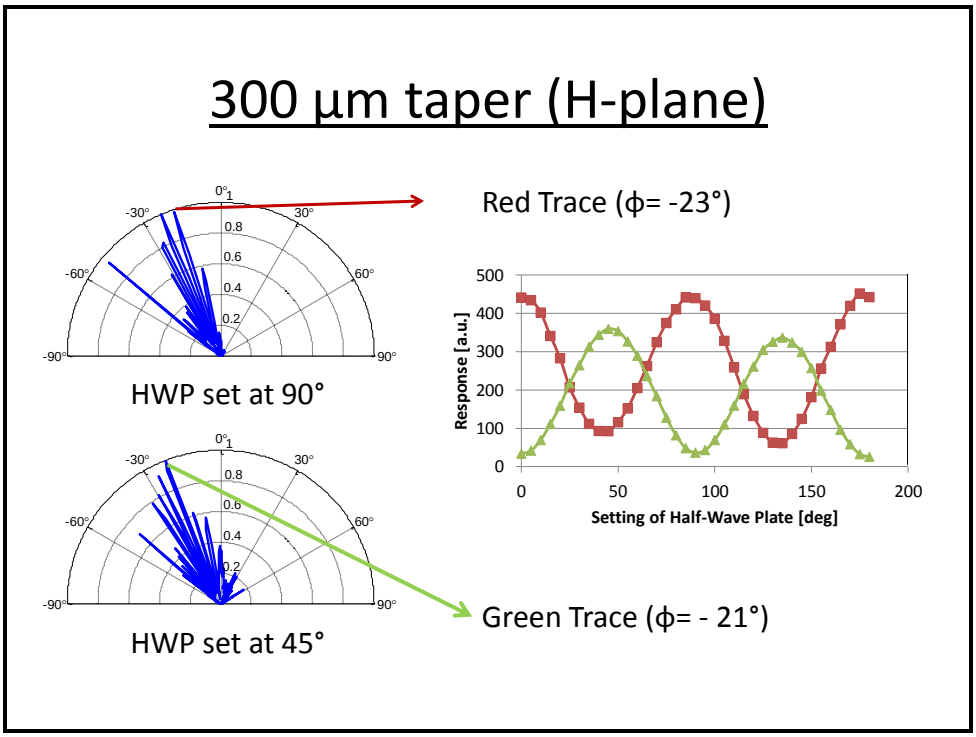

Figure 41. An example of multiple polarization states for a single antenna.

According to Lee and Simons, these peculiarities are to be expected from leaky antennas. They claim, "leaky waves cannot be supported in terms of TE or TM waves along, but by hybrid modes involving TE-TM coupling" [8]. However, no source in the references explains what antenna factors influence the polarization rejection of the leaky wave antenna. Additionally, waveport analysis in HFSS is limited to TE and TM polarizations. Other excitation methods will need to be developed in an attempt at modeling the correct polarization rejection. Successful, analytical prediction of the maximum and minimum polarization responses for a given leaky antenna would greatly improve our understanding of their operating mechanisms.

8.2 Achieving Endfire Operation

The condition for the TSA to act as an endfire antenna is that the phase velocity in the slot must equal the speed of light. This is achieved by either minimizing the effective index of the substrate, or encapsulating the antenna in a substance so that the substrate and the superstrate have the same index. As alluded to in chapter 6, most of the work in the microwave spectrum has focused on minimizing the index of the substrate. For infrared frequencies, the substrate study at the end of chapter 6 found that encapsulating the antenna in BCB was an effective means of improving the antenna's performance, but did not achieve endfire operation. A reason for this off-endfire operation is the substrate's effective index remains higher than the superstrate's effective index because of the large index of the actual substrate, the silicon wafer.

Understanding the reason for off-endfire operation provides four solutions to achieve endfire operation. First, new materials can be used for a thin film and substrate. Any reduction in the effective index of the substrate should result in a corresponding move in the radiation pattern toward endfire. Such materials exist – for example, aerogel is known to have an index close to 1, but is challenging to apply and its structural integrity in this application is suspect. Therefore, a low index film, though valuable, is not readily available.

In an attempt to reduce the index of the substrate, I attempted to place devices on zinc sulfide windows. I was unsuccessful because zinc sulfide has different properties than silicon. Because zinc sulfide is an insulator, it will develop localized charge on its surface during electron beam lithography. The effects of this charging can be minimized by thermally depositing 30 nm of chromium over the resist before conducting lithography, then etching the chromium away prior to developing the resist. My devices were destroyed by delaminating of

the BCB. It is unclear whether this delaminating was caused by the application of the chrome etch or was a result of the poor adhesive properties of zinc sulfide.

Second, a thicker film on the substrate will reduce the substrate's effective index. Experiments show that an increase of thickness in BCB from 1.6 μm to 2.1 μm (by applying two layers of BCB) did not produce observable shifts in the pattern. Thus, the increased thickness would have to be several microns. This was not a possibility with our version of BCB (Cyclotene 3022-35), but greater thicknesses are available such as Cyclotene 3022-63, which professes a thickness of 16.5 microns at a similar spin speed. This thickness could be applied in two layers, achieving 25-33 microns of BCB separation between the antenna and the silicon. Using this thicker layer should result in minimal contribution to the effective index, and thus will reduce the effective index of the substrate.

The third method is related to the overcoating method attempted in chapter 7. The addition of a superstrate was an attempt to immerse the antenna in a constant index. There are several drawbacks to the method developed, all related to dipping the device into wet BCB. First, the solvents were baked out of the BCB using the energy of the laser. This results in non-uniform, non-controllable coatings. Secondly, the BCB was baked in an oxygen environment, when it should be cured in a nitrogen environment. The presence of oxygen changes the absorptive spectrum of the BCB (although it is not clear what effect this has at 10.6 μm). Solutions to these problems include determining if the diode will withstand the nitrogen environment hard-cure temperature of 250 C, which will allow proper curing of both the substrate and superstrate films. It will also allow the superstrate to be spun onto a silicon wafer, thus ensuring uniform application. Prior to its curing, the superstrate could be affixed to the

device/substrate, forcing a symmetric substrate-superstrate configuration. This symmetry should ensure endfire operation.

The fourth method, and the least obvious, is the adaptation of techniques used at microwave frequencies. These techniques include placing plasmonic waveguides on the substrate below the film, creating perfect magnetic conducting structures on the silicon, and the milling of the substrate to reduce its effective index. These are novel ideas that met varying degrees of success. These techniques will require many attempts and are not guaranteed to succeed. If they were successful, though, they could solve the problem of the high index substrate and add significantly to the knowledge of how devices work at infrared frequencies.

It is my opinion that the solution is some combination of these four methods. Of particular interest is a combination of the thick substrate film and the uniform superstrate configuration. This would minimize the effects of the silicon, while encapsulating the antenna in BCB. The only required resource is the thicker BCB, making this a very attractive solution to achieve endfire operation.

8.3 Quantification of Broadband Operation

One of the claims of TSAs is that they operate over a broad bandwidth. The Vivaldi Aerial [1] had a bandwidth of two octaves. The benefits of such a large bandwidth for infrared detection would further the demand for tapered slot antennas. However, we have been unable to quantify how broadband the infrared TSA actually is because of the absorptive spectrum of BCB (Fig. 42). Note that the low absorption window near 10.6 μm is very narrow (approximately 2 μm). This inhibits the usefulness of BCB for broadband applications, and prevents a quantification of the broadband capabilities of the infrared TSA.

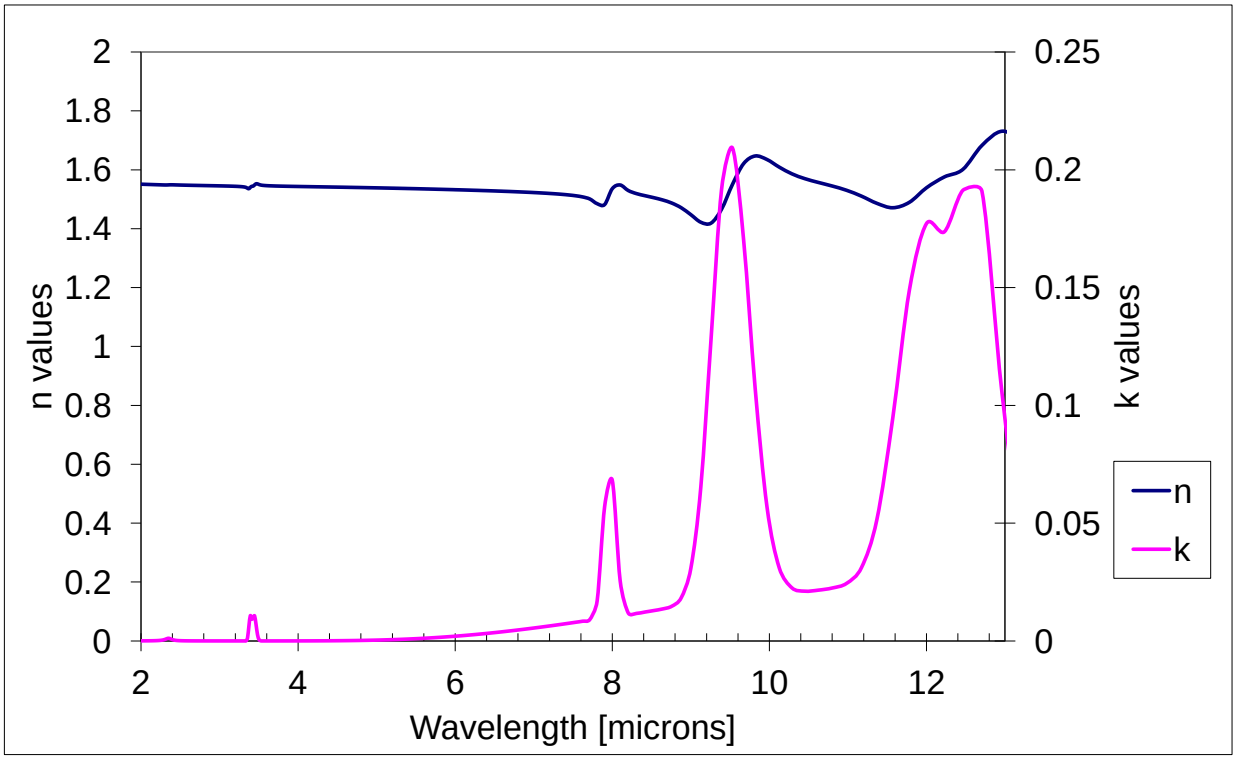

Figure 42. The complex refractive index for BCB at infrared wavelengths.

There are two solutions to this. The first is to continue modeling efforts in HFSS, substituting BCB with some material with constant n and k values over all frequencies. While this could be accomplished in a relatively short time, it lacks the actual data to validate the model. The second solution involves using esoteric films in the place of BCB. One candidate is polyethylene which has a transmission window from 7 μm to 13.5 μm [68]. Its transmission spectrum is shown in Fig. 43. This is not necessarily an easy task, as polyethylene is difficult to work with [69]. However, once an application process is developed, a wide range of infrared sources could be used to verify model results.

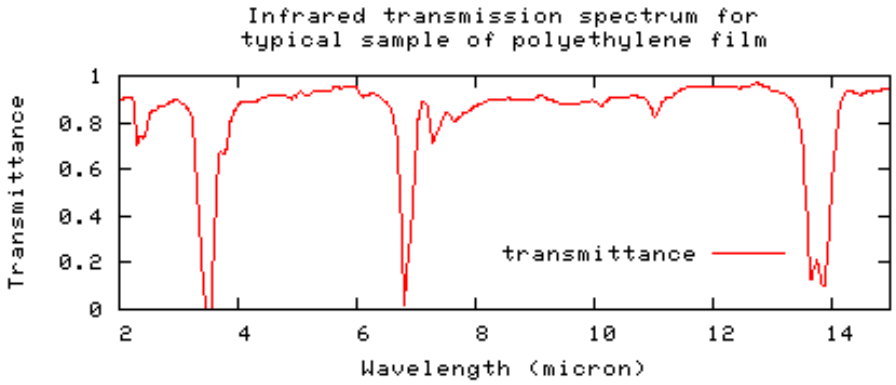

Figure 43. The transmission spectrum for polyethylene.

8.4 Beyond the V-LTSA Geometry: Plug-and-Play Diode Fabrication

The V-LTSA was developed as a solution to the lithographic difficulties inherent in writing large patterns and small patterns in proximity to each other, as discussed in Chapter 2. If the diode could be added at a different step in the process, the shape and materials used in the TSA would not be limited to thin lines. This improvement would not only benefit TSA fabrication, but many other elements such as energy harvesters and logarithmic antennas.

Several attempts were made to place the diode inside the slot after then antenna bodies were present (Fig. 44). The antenna planes were gold, and the diode strip was the standard aluminum and platinum diode introduced in Chapter 2. Although the alignment for these devices was very good, the vast majority resulted in open circuits when tested electrically. This is a result of either the platinum not surviving the lift off procedure, or a gold-aluminum-aluminum oxide alloy forming, also known as the purple plague. A study was conducted showing that aluminum could provide a short across the planes if it were at least 200 nm wide, which is 120 nm wider than the conventional diodes.

A separate discovery by Brown and Kinzel [70] reopens the possibility of placing diodes after the antenna bodies are fabricated. They discovered that diodes could be constructed on microstrips up to 500 nm wide. Not only would this ensure electrical contact between the gold and the aluminum, but it would also improve the probability that platinum would survive the lift-off process. This would allow wider diodes to be placed into the slot region of the antennas, providing the freedom to arrange the antenna bodies in any fashion.

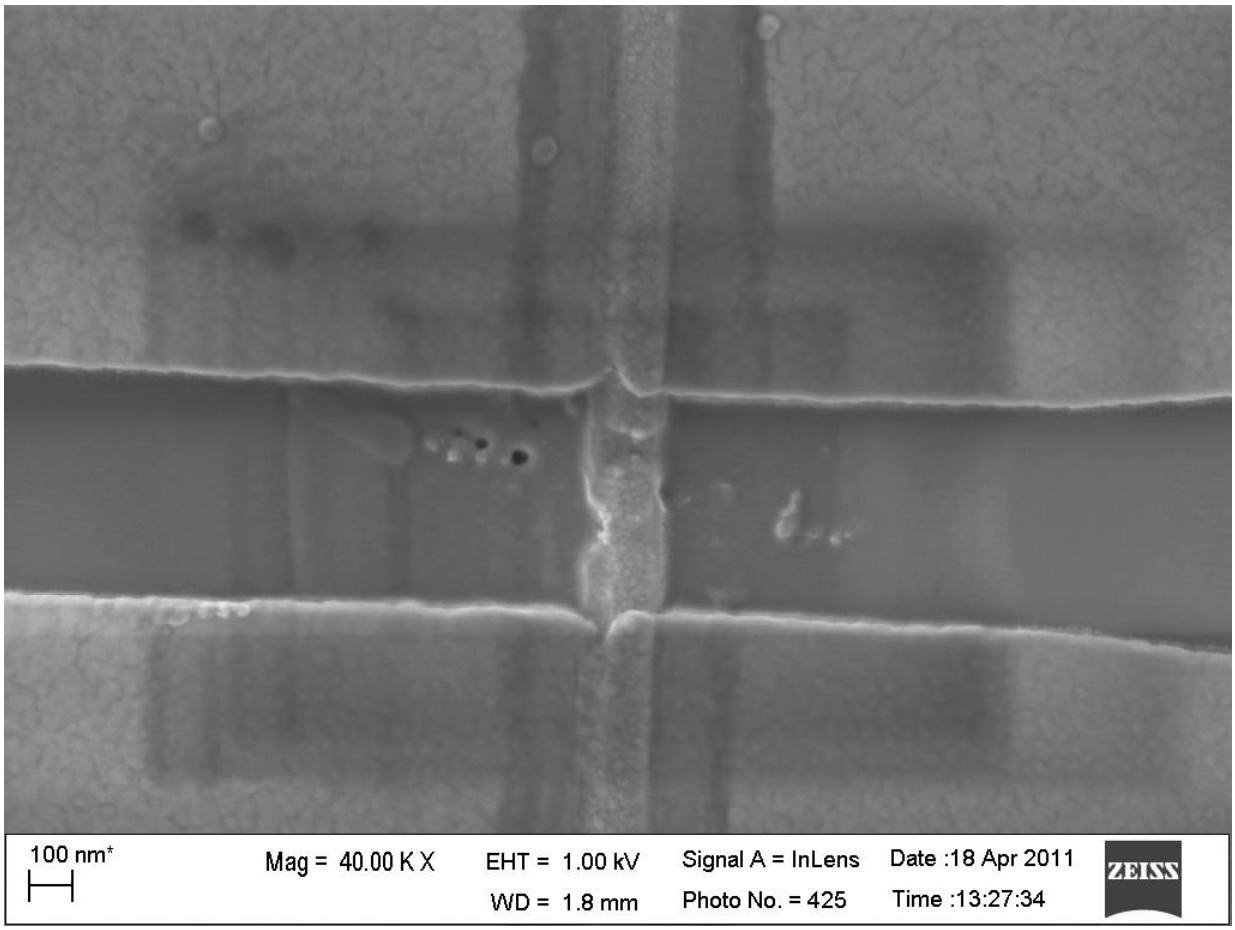

Figure 44. Attempted plug-and-play diode fabrication.

REFERENCES

[1] P.J. Gibson, "The Vivaldi aerial", in *Procedures of the 9th European Microwave Conference*, Brighton, UK, 101-105, 1979.

[2] S.N. Prasad and S. Mahapatra, "A novel MIC slot line aerial", in *Procedures of the 9th European Microwave Conference*, Brighton, UK, 120-124, 1979.

[3] K. Sigfrid Yngvesson, D. Schaubert, T. Korzenioski, et al, "Endfire tapered slot antennas on dielectric substrates", *IEEE Transaction on Antennas and Propagation*, **AP-33**, 12, 1392-1400, 1985.

[4] S.I. Svechnikov, O.V. Okunev, et al., "2.5THz NbN hot electron mixer with integrated tapered slot antenna", *IEEE Transaction on Applied Superconductivity*, **7**, 2, 3548-3551, 1997.

[5] M. Greenberg, K. Virga and C. Hammond, "Performance characteristics of the dual exponentially tapered slot antenna (DETSA) for wireless communications applications", *IEEE Transactions on Vehicular Technology*, **52**, 2, 305-312, 2003.

[6] H. Xu, H. Zhang, J. Wang, L. Ma, "A new tapered slot antenna with symmetrical and stable radiation patterns", *Progress in Electromagnetics Research Letters*, **5**, 35-43, 2008.

[7] S. Nikalaou, G. Ponchak, J. Papapolymerou, M Tentzeris, "Double exponentially tapered slot antenna (DETSA) on liquid crystal polymer (LCP) for UWB applications", *Antennas and Propagation Society International Symposium 2005 (IEEE)*, **2A**, 623-626, 2005.

[8] R.Q. Lee and R.N. Simons, "Tapered slot antennas", Advances in Microstrip and Printed Antennas, ed. Kai Fong Lee and Wei Chen, Wiley and Sons: New York, 1997, pp. 443-514.

[9] J. Muldavin and G. Rebeiz, "Millimeter-wave tapered slot antennas on synthesized low permittivity substrates", *IEEE Transactions on Antennas and Propagation*, **47**, 8, 1276-1280, 1999.

[10] N. Chen, C. Chuang, and J. Shi, "A W-band linear tapered slot antenna on rectangular-grooved silicon substrate", *IEEE Antennas and Wireless Propagation Letters*, **6**, 90-92, 2007.

[11] J. Irzk and G. Rebeiz, "Millimeter-wave Fermi tapered slot antennas on micromachined silicon substrates", *IEEE Transactions on Antennas and Propagation*, **50**, 3, 379-383, 2002.

[12] S. Cohn, "Slot line on a dielectric substrate", *IEEE Transactions on Microwave Theory and Techniques*, **MTT-17**, 10, 768-778, 1969.

[13] R. Janaswamy and D. Schaubert, "Characteristic impedance of a wide slotline on low-permittivity substrates", *IEEE Transactions on Microwave Theory and Techniques*, **MTT-34**, 8, 900-902, 1986.

[14] R. Janaswamy and D. Schaubert, "Dispersion characteristics for wide slotlines on low-permittivity substrates", *IEEE Transactions on Microwave Theory and Techniques*, **MTT-33**, 8, 723-726, 1985.

[15] A. Snyder and J. Love, "Goos-Haenchen shift", *Applied Optics*, **15**, 1, 236-238, 1976.

[16] R. Janaswamy and D. Schaubert, "Analysis of the tapered slot antenna", *IEEE Transaction on Antennas and Propagation*, **AP-35**, 9, 1058-1065, 1987.

[17] F. Gonzalez, J. Alda, J. Simon, J. Ginn, and G. Boreman, "The effect of metal dispersion on the resonance of antennas at infrared frequencies," *Infrared Physics & Technology*, **52**, 1, 48-51 2009.

[18] K.S. Yngvesson, T.L. Korzeniowski, Y.S. Kim, E. Kollberg, and J. Johansson, "The tapered slot antenna – a new integrated element for millimeter-wave applications", *IEEE Transactions on Microwave Theory and Techniques*, **37**, 2, 365-374, 1989.

[19] P. Acharya, J. Ekstrom, S. Gearheart, S. Jacobsson, J. Johansson, E. Kollberg, G Rebeiz, "Tapered slotline antennas at 802 GHz", *IEEE Transactions on Microwave Theory and Techniques*, **41**, 10, 1715-1719, 1993.

[20] M. Lazaro and R. Judaschke, "A 150-GHz CPW-fed tapered slot antenna", *IEEE Microwave and Wireless Components Letters*, **14**, 2, Feb 2004, 62-64, 2004.

[21] T.G. Lim, H. N. Ang, I.D. Robertson, and B.L. Weiss, "Tapered slot antenna using photonic bandgap structure to reduce substrate effects", *Electronic Letters*, **41**, 7, 393-394, 2005.

[22] U. Kotthaus and B. Vowinkel, "Investigation of planar antennas for submillimeter receivers", *IEEE Transactions on Microwave Theory and Techniques*, **37**, 2, 375-380, 1989.

[23] Yao Yuan, C. Wenhau, H. Bin, F. Zhenghe, Z. Zhijun, "Analysis and design of tapered slot antenna for ultra-wideband applications", *Tzinghua Science and Technology*, **14**, 1, 1-6, 2009.

[24] H. Oraizi and S. Jam, "Optimum design of tapered slot antenna profile", *IEEE Transactions on Antennas and Propagation*, **51**, 8, 1987-1995, 2003.

[25] J.A. Dionne, L. Sweatlock, H. Atwater, A. Polman, "Plasmon slot waveguides: toward chip-scale propagation with subwavelength-scale localization", *Physical Review*, **B73**, 3, 035407-1-9, 2006.

[26] J. Wen, S. Romanov, U. Peschel, "Excitation of plasmonic waveguides by nanoantennas", *Optics Express*, **17**, 8, 5925-5932, 2009.

[27] T. Itoh and R. Mittra, "Dispersion characteristics of slot lines", *Electronic Letters*, **7**, 13, 364-365, 1971.

[28] T. Mandviwala, B. Lail, G. Boreman, "Infrared-frequency coplanar striplines; design, fabrication, and measurements", *Microwave and Optical Technology Letters*, **47**, 1, 17-20, 2005.

[29] J. Bean, B. Tiwari, G. Bernstein, P. Fay, W. Porod, "Thermal infrared detection using dipole antenna-coupled metal-oxide-metal diodes", *Journal of Vacuum Science and Technology*, **B27**, 1, 11-14, 2009.

[30] A. Sanchez, C.F. Davis, K.C. Liu, A. Javan, "The MOM tunneling diode: theoretical estimate of its performance at microwave and infrared frequencies", *Journal of Applied Physics*, **49**, 10, 5270-5277, 1978.

[31] J. Bean, B. Tiwari, G. Szakmany, G. Bernstein, P. Fay, W. Porod, "Antenna length and polarization response of antenna-coupled MOM diode infrared detectors", *Infrared Physics and Technology*, **53**, 3, 182-185, 2010.

[32] J. Bean, A. Weeks, G. Boreman, "Performance optimization of antenna-coupled Al/AlOx/Pt tunnel diode infrared detectors", *Journal of Quantum Electronics*, **47**, 1, 126-135, 2011.

[33] B. Tiwari, J. Bean, G. Szakmany, G. Bernstein, P. Fay, W. Porod, "Controlled etching and regrowth of tunnel oxide for antenna-coupled metal-oxide-metal diodes", *Journal of Vacuum Science and Technology*, **B27**, 5, 2153-2160, 2009.

[34] B. Slovick, J. Bean, P. Krenz, and G. Boreman, "Directional control of infrared antenna-coupled tunnel diodes", *Optics Express*, **18**, 20, 20960-20967, 2010.

[35] P. Hobbs, R. Laibowitz, F. Libsch, N. LaBianca, P. Chiniwalla, "Efficient waveguide integrated tunnel junction detectors at 1.6 μm", *Optics Express*, **15**, 25, 16376-16389, 2007.

[36] J. Bean, B. Slovick, G. Boreman, "Influence of substrate configuration on the angular response pattern of infrared antennas", *Optics Express*, **18**, 21, 21705-21713, 2010.

[37] Ansoft HFSS Users Guide for Software Version 10.0, ed. Ansoft Corporation, Rev.1.0, 21 June 2005.

[38] P. Krenz, B. Slovick, J. Bean, G. Boreman, "Alignment procedure for radiation pattern measurement of antenna-coupled infrared detectors", *Optical Engineering*, **49**, 3, 033607, 2010.

[39] G.E. Evans, Antenna Measurement Techniques, Artech House: Boston, 1990.

[40] Electromagnetic Horn Antennas, ed. A.W. Love, IEEE Press: New York, 1976.

[41] E. Dereniak and G. Boreman, Infrared Detectors and Systems. New York, NY:John Wiley, 1996, p. 413.

[42] F. González and G. Boreman, "Comparison of dipole, bowtie, spiral and log-periodic IR antennas," *Infrared Physics and Technology*, **46**, 5, 418-428, 2005.

[43] T. Hwang, D. Rutledge and S. Schwarz, "Planar sandwich antennas for submillimeter applications", *Applied Physics Letters*, **34**, 1, 9-11, Jan. 1979.

[44] Gibson reported a 2-octave (8-40GHz) device.

[45] J. J. Lee and S. Livingston, "Wide band bunny-ear radiating element," in *Proc. IEEE Antennas Propagation Soc. Int. Symp.*, Ann Arbor, MI, 1604–1607, 1993.

[46] M. Fox, Optical Properties of Solids, 2nd ed., Oxford, U.K.: Oxford Press, 2010, p.216.

[47] E.C. Kinzel, J.C. Ginn, R.L. Olmon, D.J. Shelton, B.A. Lail, I. Brenner, M.B. Sinclair, M.B. Raschke, G.D. Boreman, "Phase resolved near-field mode imaging for the design of frequency-selective surfaces", *Optics Express*, **20**, 11986-11993, 2012.

[48] R. Olmon, P. Krenz, A. Jones, G. Boreman, M. Raschke, "Near-field imaging of optical antenna modes in the mid-infrared", *Optics Express*, **16**, 25, 20295-20305, 2008.

[49] R. Olmon, P. Krenz, B. Lail, L. Saraf, G. Boreman, M. Raschke, "Nano-optical vector network analyzer", *Laser and Electro-optics (CLEO) and Quantum Electronics and Laser Science Conference (QELS)*, 16-21 May 2010, San Jose, CA.

[50] L. Tang, S. E. Kocabas, S. Latif, A. K. Okyay, D.-S. Ly-Gagnon, K. C. Saraswat, and D. A. B. Miller, "Nanometre-scale germanium photodetector enhanced by a near-infrared dipole antenna", *Nature Photonics* **2**, 226-229, 2008.

[51] I. Wilke and W Herrmann, "Integrated nanostrip dipole antennas for coherent 30 THz infrared radiation", *Applied Physics B* **95**, 87-95, 1994.

[52] R. Corkish, M.A. Green, T. Puzzer, "Solar energy collection by antennas", *Solar Energy* **73**, 395-401, 2002.

[53] J. Ginn, B. Lail, J. Alda, G. Boreman, "Planar infrared binary phase reflectarray", *Opt. Lett.* **33**, 779-781, 2008.

[54] D.A. Genov, A.K. Sarychev, V.M. Shalaev, A. Wei, "Resonant field enhancements from metal nanoparticle arrays", *Nano. Lett.*, **4**, 153-158, 2004.

[55] J. Alda, J.M. Rico-Garcia, J.M. Lopez-Alonso, G. Boreman, "Optical antennas for nano-photonic applications", *Nanotechnology*, **16**, 230-234, 2005.

[56] F. Neubrech, D. Weber, R. Lovrincic, A. Pucci, M. Lopes, T. Toury, and M. Lamy de La Chapelle, "Resonances of individual lithographic gold nanowires in the infrared", *Applied Physics Letters* **93**, 163105, 2008.

[57] L.A. Florence, B.A. Slovick, E.C. Kinzel, J.A. Bean, G.D. Boreman, "Infrared linear tapered slot antenna", *IEEE Antennas and Wireless Propagation Letters*, **10**, 1299-1301, 2011.

[58] P.M. Krenz, R.L. Olmon, B.A. Lail, M.B. Raschke, G.D. Boreman, "Near-field measurement of infrared coplanar strip transmission line attenuation and propagation constants", *Optics Express* **18**, 21678-21686, 2010.

[59] M. Schnell, P. Alonso-Gonzalez, L. Arzubiaga, F. Cananova, L.E. Hueso, A. Chuvillin, R. Hillenbrand, "Nanofocusing of mid-infrared energy with tapered transmission lines", *Nature Photonics* **5**, 283-287, 2011.

[60] J. Dorfmüller, D. Dregely, M. Esslinger, W. Khusin, R. Vogelgesang, K. Kern, H Giessen, "Near-field dynamics of optical Yagi-Uda nanoantennas", *Nano. Lett.* **11**, 2819-2824, 2011.

[61] I.K. Kim, N. Kidera, S. Pinel, J. Papapolymerou, J. Laskar, J. Yook, and M.Tentzeris, "Linear tapered cavity-backed slot antenna for millimeter-wave LTCC modules", *IEEE Antennas and Wireless Propagation Letters*, **5**, 175-178, 2006.

[62] T. Zentgraf, J. Dorfmüller, C. Rockstuhl, C. Etrich, R. Vogelgasang, K. Kern, T. Pertsch, F. Lederer, H. Giessen, "Amplitude- and phase-resolved optical near-fields of split-ring-resonator-based metamaterials", *Opt. Lett.* **33**, 848-850, 2008.

[63] A. Huber, N. Ocelic, D. Kazantsev, R. Hillenbrand, "Near-field imaging of mid-infrared surface phonon propagation", *Appl. Phys. Lett.* **87**, 081103, 2005.

[64] N. Ocelic, A. Huber, R. Hillenbrand, "Pseudoheterodyne detection for background-free near-field spectroscopy", *Appl. Phys. Lett.* **89**, 101124, 2006.

[65] F. Keilmann, R. Hillenbrand, Near-field microscopy by elastic light scattering from a tip, *Phil. Trans. R. Soc. Lond. A*, **362**, 787-805, 2004.

[66] L.A. Florence, E.C. Kinzel, R. L. Olmon, J.C. Ginn, M.B. Raschke, G.D. Boreman, "Phase resolved near-field imaging of propagating waves in infrared tapered slot antennas", *Journal of Infrared Physics and Technology* (to be published).

[67] I. Codreanu, F. González, and G. Boreman, "Detection mechanisms in microstrip antenna-coupled infrared detectors," *Infrared Physics and Technology* **44**, 155–163, 2003.

[68] R.T. Conley, Infrared Spectroscopy, 2nd Ed., Allyn and Bacon: Boston, 1972, p. 266., as cited at http://people.csail.mit.edu/jaffer/FreeSnell/polyethylene.html

[69] J.C. Ginn, verbal conversation, May 9, 2012.

[70] E.C. Kinzel, verbal conversation, July 14, 2011.